Lithosphere

Research Article

The Anatomy and Origin of a Synconvergent Grenvillian-Age Metamorphic Core Complex, Chottanagpur Gneiss Complex, Eastern India

Nicole Sequeira (ID),[1] **Souradeep Mahato,**[1] **Jeffrey M. Rahl,**[2] **Soumendu Sarkar,**[1] **and Abhijit Bhattacharya**[1]

[1]Department of Geology and Geophysics, Indian Institute of Technology, Kharagpur 721 302, India
[2]Department of Geology, Washington and Lee University, 204 West Washington Street, Lexington, VA 24450, USA

Correspondence should be addressed to Nicole Sequeira; nix.seq@gmail.com

Amphibolite facies supracrustal rocks interleaved with granite mylonites constitute a shallowly dipping carapace overlying granulite facies anatectic basement gneisses in the Giridih-Dumka-Deoghar-Chakai area that spans ~11,000 km^2 in the Chottanagpur Gneiss Complex (CGC). Steep N-trending tectonic fabrics in the gneisses include recumbent folds adjacent to the overlying carapace. The basement and carapace are dissected by steep-dipping sinistral shear zones with shallow/moderately plunging stretching lineations. The shear zones trend NNE in the north (north-down kinematics) and ESE in the south (south-down kinematics). Chemical ages in metamorphic monazites in the lithodemic units are overwhelmingly Grenvillian in age (1.0–0.9 Ga), with rafts of older domains in the basement gneisses (1.7–1.45 Ga), granitoids (1.4–1.3 Ga), and the supracrustal rock (1.2–1.1 Ga). P-T pseudosection analysis indicates the supracrustal rocks within the carapace experienced postthrusting midcrustal heating (640–690°C); the Grenvillian-age P-T path is distinct from the existing Early Mesoproterozoic P-T path reconstructed for the basement gneisses. Quartz opening angle thermometry indicates that high temperature (~600°C) persisted during deformation in the southern shear zone. Kinematic vorticity values in carapace-hosted granitoid mylonites and in steep-dipping shear zones suggest transpressional deformation involved a considerable pure shear component. Crystallographic vorticity axis analysis also indicates heterogeneous deformation, with some samples recording a triclinic strain. The basement-carapace composite was extruded along an inclined channel bound by the steep left-lateral transpressional shear zones. Differential viscous extrusion during crustal shortening coupled with the collapse of the thickened crust caused midcrustal flow along flat-lying detachments in the carapace.

1. Introduction

The formation of Metamorphic Core Complexes (MCCs) is conventionally related to extensional tectonic processes ([1] and references therein), although proposed models vary in the details [2–9]. In addition to regions dominated by extension, such as the Basin and Range province, MCCs have been reported from accretionary margins [10] and in convergent regimes [1, 11, 12]. Despite the convergent nature of these tectonic settings, MCC development is associated with extension-related processes such as slab rollback, intrusion driven extension [13], or orogenic collapse under fixed boundary conditions or slow plate convergence [14]. Searle and Lamont [15] demonstrate that MCCs can form in entirely compression regimes unaffected by any extensional tectonism.

Synconvergent to postconvergent gravitational collapse of a previously thickened orogenic crust [16–23] may lead to the development of extensional shallow-dipping midcrustal detachment zones [19, 24–30] that may exhume deep-

seated lower crustal rocks within a MCC. Long et al. [31] demonstrate that regions of upper crustal thickening directly control the spatial location of synorogenic extension. Additionally, vertical partitioning of strain in the crust during convergence can localize extension in the upper crust and contraction in the ductile lower crust (e.g., [1, 7, 32–37]).

The presence of regional scale strike-slip dominated shear zones is noted in a number of MCCs [10, 38–45]. Although these shear zones are known to aid exhumation of the deep crustal rocks [6, 46–54], limited data exist on the field relations of these shear zones and their role in the formation of MCCs [55].

This work documents possibly the first MCC recognized in peninsular India (cf. Figure 2 of [1]), based on detailed structural mapping in the eastern part of the Chottanagpur Gneiss Complex (CGC) (Figure 1). The proposed Early Neoproterozoic MCC lies in the foreland region of a contemporaneous convergent boundary between the Meso-/Neoproterozoic CGC and the Meso-/Neoarchean Singhbhum Craton in the south (Figure 1(a)) and is closely associated with steep-dipping transpressional shear zones. Kinematic analyses coupled with crystallographic data, monazite dating, and P-T pseudosection analyses illustrate the evolution of the proposed MCC.

2. Geological Background

The Precambrian crystalline rocks of the CGC constitute a vast area (~80,000 sq. km). The rocks may be classified into three lithodemic units: (i) regionally extensive basement anatectic gneisses that include granulite facies felsic (charnockite-enderbite) orthogneisses, garnet-biotite-sillimanite-K-feldspar-bearing metapelite, calc silicate granulite, mafic granulite, massif anorthosites, and silica undersaturated syenites; (ii) blastoporphyritic granitoids structurally varying from massive to foliated to mylonitic rocks predominant in the CGC; and (iii) lower/middle-amphibolite facies supracrustal rocks that include muscovite-biotite schist (with rare garnet and sillimanite), micaceous and ferruginous quartzites, amphibolites (hornblende-plagioclase±epidote), and minor amounts of metamarls and metadolomite ([56, 57] and references therein). The high-grade gneisses and granulites occur as outcrop scale enclaves within the blastoporphyritic granitoids that comprise the basement of the CGC [58–61]. The supracrustal rocks are prominently exposed in E-trending belts that coincide with topographic highs along and neighboring regional scale curvilinear ductile shear zones that trend E/ENE in central/northern CGC and E/ESE in southern CGC [62] (Figure 1(a)). The three lithodemic units are unconformably overlain by rift-related Gondwana basins that host Permo-Carboniferous to Early Cretaceous glacial-glaciogenic sediments that transition to fluvial sedimentary successions [63]. The Gondwana basin sediments are intruded by mafic and lamprophyre dykes and overlain by basalt flows [64, 65]. This study investigates a quadrangular area in the eastern part of the CGC covering ~11,000 km^2 near the towns of Deoghar, Dumka, Giridih, and Chakai (Figure 1(b)).

U-Pb zircon geochronology [66–70] and pooled monazite chemical ages [59] suggest the anatectic basement gneisses of the CGC are the oldest (1.60–1.45 Ga) lithodemic unit in the study area. This age range corresponds to high-grade metamorphism-anatexis [61, 66, 69, 71] and emplacement of felsic intrusives (Mukherjee et al. [67, 68]. Considerable variations exist in the U-Pb zircon ages obtained by Mukherjee et al. [67–69] in the felsic lithologies in the Dumka-Deoghar area. Near-concordant and discordant U-Pb systematics in zircons from a charnockite gneiss/felsic orthogneiss sample (AS-100) yield an upper intercept age of 1450 Ma (emplacement age) and a lower intercept 943 Ma age from the intermittent and weak metamorphic overgrowth of zircon rims [67]. These authors suggest the weak Early Neoproterozoic overgrowths relate to a granulite-facies clockwise P-T path culminating with near-isothermal decompression in the retrograde sector. This contradicts the earlier findings [60, 61, 66, 72] that the granulite facies metamorphism in the basement gneisses is at least older than 1.4 Ga. It will be shown later that the field relationship and mesoscale structures adopted by Mukherjee et al. [67] in their interpretation are contentious.

In areas neighboring Dumka, Mukherjee et al. [68] report two amphibole-biotite-gneiss/granite samples (AS-114A and AS-34/1) with a mean U-Pb zircon age of 1465 ± 17 Ma; this age is interpreted to correspond with the emplacement of the rocks. Based on the Lu-Hf isotopic compositions in zircon and major and trace element geochemistry of similar rocks, Mukherjee et al. [68] suggest that the protolith (ferroan A-type granitoid) for the rocks was derived from a Paleoproterozoic crustal source. Mukherjee et al. [69] determine U-Pb zircon ages of two biotite-amphibole-garnet bearing felsic augen gneisses from Deoghar, e.g., 1709 ± 17 Ma for AS-37 and 1626 ± 17 for AS-83A; the authors suggest that these ages represent the time of ultrahigh T granulite facies metamorphism.

There are no existing age data available in the amphibolite facies supracrustal rocks near Dumka. However, in the southern and central CGC, monazite chemical ages in the muscovite-biotite schists show two nonoverlapping age groups: 1300–1200 Ma ages are found in strongly embayed and fragmented cores mantled by younger (1050–880 Ma) metamorphic rims [59, 61, 62, 73, 74]. Metamorphic P-T path reconstructions in the supracrustal rocks in central CGC are not available.

The Early Neoproterozoic metamorphism is broadly coeval with the emplacement (1.1–0.9 Ga) of the expansive blastoporphyritic granitoids throughout the CGC ([66], and references therein; [58, 61, 62, 71, 73–75]). Goswami and Bhattacharyya [75] used petrographic and geochemical characters (major and trace elements, mineral chemistry, and $^{87}Sr/^{86}Sr$ ratios) to classify such granitoids in the 1071 ± 64 Ma Raghunathpur batholith to be postcollisional shoshonites formed due to the delamination of the subducting slab.

3. Field Setting

The Giridih-Dumka-Deoghar-Chakai area exposes the three lithodemic units of the CGC, i.e., the granulite facies gneisses,
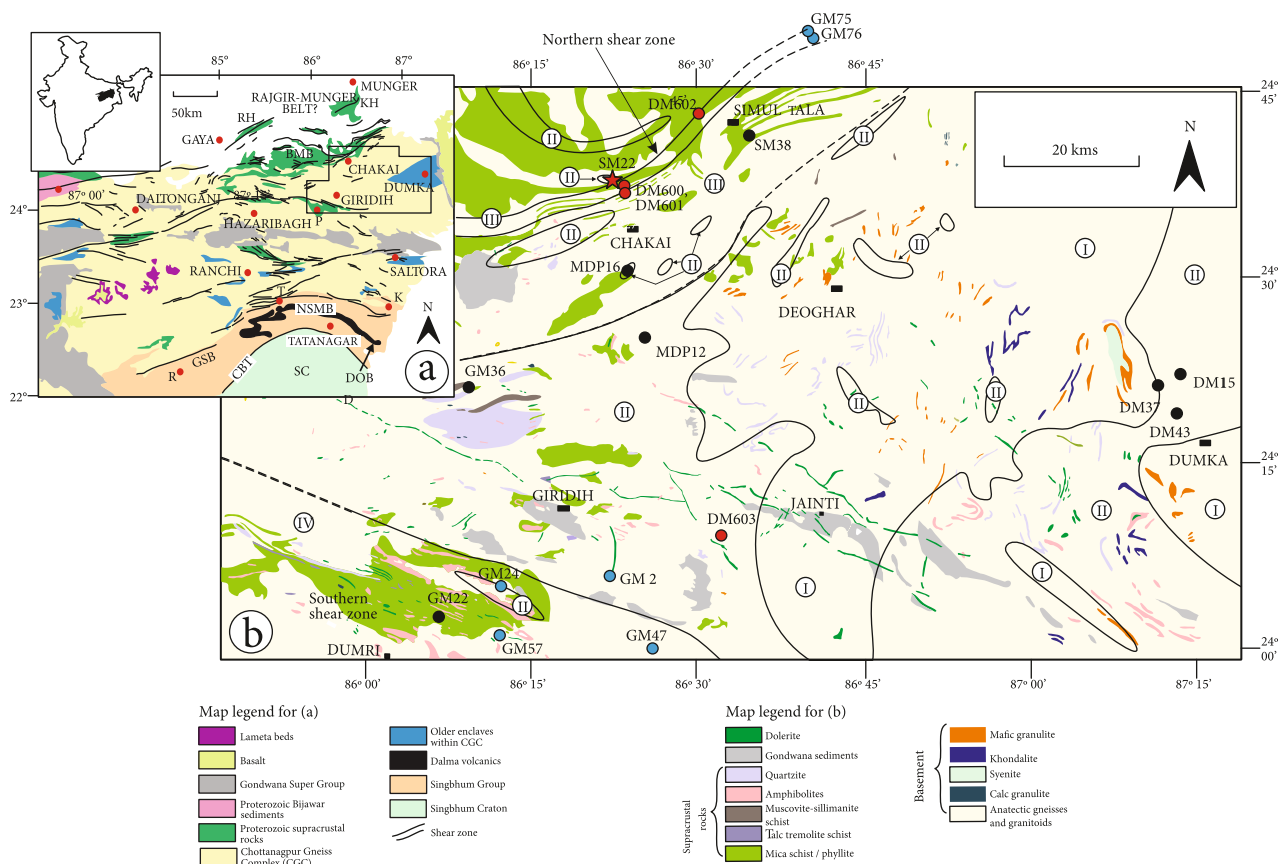
FIGURE 1: (a) Simplified geological map of the Chottanagpur Gneiss Complex (CGC), eastern India, showing the network of shear zones within the CGC [62]. The box shows the Giridih-Dumka-Deoghar-Chakai area. The following acronyms are used: BMB: Bihar Mica Belt; RH: Rajgir Hills; KH: Kharagpur Hills; P: Paresnath Hills; NSMB: North Singhbhum Mobile Belt; GSB: Gangpur Schist Belt; DOB: Dalma Ophiolite Belt; SC:Singhbhum Craton. The Rajgangpur- (R-)Tamar- (T-) Katra (K) shear zone demarcates the CGC-NSMB accretion zone. The Copper Belt Thrust (CBT) marks the NSMB-SC accretion zone. The inset map of India shows the location of the CGC (filled area). (b) Disposition of the lithodemic units in the Giridih-Dumka-Deoghar-Chakai area. Based on our independent observations, the lithologies in the Geological Survey of India District Resource Maps of Devghar [174], Giridih [175], Dumka [176], Banka [177], and Jamui [178] are modified. Boundaries between Domains I–IV (details in Figures 2(a) and 2(b); refer to text) are shown on the map. Locations of samples used for monazite age determinations (black circles), EBSD analyses (blue circles), kinematic vorticity analyses (red circles), and P-T pseudosection analysis (red star) are indicated.

blastoporphyritic granitoids, and amphibolite facies supracrustal rocks (Figure 1(b)). The blastoporphyritic granitoids in the area are either pink or grey in color and commonly contain K-feldspar porphyroclasts and submeter to kilometer scale enclaves of the gneisses. The supracrustal rocks are restricted to the northern and southern parts of the area (Figure 1(b)). The Gondwana Supergroup sediments unconformably overlie the three lithodemic units.

As the anatectic gneisses are the oldest lithodemic unit within the CGC, they record all of the deformation events affecting the CGC (Table 1). Four structural domains are identified, based on observations in 1002 field stations (Figure 2). Domain I outcrops in the east-central part of the area, lacks supracrustal rocks, and is dominated by basement gneisses and granitoids that exhibit steeply dipping (>50°), sinuous, N-trending tectonic fabrics. The three other domains include blastoporphyritic granitoids and supracrustal rocks in addition to the basement anatectic gneisses. Domain II rocks in the west-central and southeastern parts

(Figure 2(a)) are characterized by shallow-dipping (dip < 35°) fabrics; these occur both in discontinuous lenses in and neighboring the northern and the southern shear zones and as irregular patches structurally overlying Domain I. Areas where these fabrics have steepened due to folding neighboring the steep-dipping shear zones are excluded from Domain II. Domain III and Domain IV are characterized by deformational structures within and near the steep shear zones that trend ENE in the north and ESE in the south. Lower hemisphere stereographic projections for the deformation fabrics in the lithodemic units within the four domains are summarized in Figure 3. The two shear zones in Domains III and IV appear to converge in the west, but deep weathering and alluvial cover obscured their projected intersection north and west of Giridih (Figure 2).

The conventional three-part classification of continental MCCs described by Platt et al. [6] consists of (1) the metamorphic core consisting of high-grade ductilely deformed metamorphic rocks, (2) the overlying detachment zone

TABLE 1: Correlation of mesoscale structures in the Giridh-Dumka-Deoghar-Chakai region.

	Basement gneisses	Supracrustal rocks	Foliated/mylonite granitoids
1.45–1.7 Ga Mesoproterozoic			
D1	Granulite facies metatexite layers (S_{N1}) in felsic gneiss, Grt-sill gneiss		
D2	Isoclinal folds (fold axis: L_{N2}) on S_{N1} in interfolial domains of sinuous and penetrative (S_{N2}) gneiss-defined layers; S_{N2} is steep-dipping and N-trending; local Grt±Opx-bearing diatexite at boudin neck in felsic gneiss; local S_{N2} Opx-bearing leucosome in mafic granulite		Older suite of granitoids shares the steep-dipping S_{N2} fabric of the gneisses defined by planar alignment of mafic Schlieren
0.9–1.1 Ga Grenvillian age			
D3	*In carapace (detachment zone)* Recumbent to gently inclined folds on S_{N2} with local development of flat-lying/shallow-dipping axial plane fabric (S_{N3}); plunge of folds (L_{N3}) varies from NW through N to SE. No evidence of anatexis *Below carapace* Unaffected	*In carapace (detachment zone)* Penetrative crenulation cleavage (S_{S2}); flat-lying/shallow-dipping; in mesoscale S_{S1} largely obliterated, but S_{S1} occurs as microscale fold hinges and oblique foliation in S_{S2} interfolial domains; L_{S2} fold axis is rare *Below carapace* Absent	*In carapace (detachment zone)* Monophase flat-lying/shallow-dipping mylonitic foliation (S_{G1}) in younger granitoids; S, S>L tectonite, stretching lineation (L_{G1}) orientations variable. Isoclinal recumbent folds in older granitoids *Below carapace* No mesoscale fabric in younger granitoids; older granitoids unaffected
D4	*In carapace (detachment zone)* Upright folds with gently plunging/subhorizontal axes (L_{N4}); ESE-/E-trending axial planes (S_{N4}). No evidence of anatexis *Below carapace* Steeply plunging folds (fold axis: L_{N4}) Rare sheath folds; ENE-/ESE-trending Axial planes (S_{N4}). No anatexis	*In carapace (detachment zone)* Upright folds with gently plunging/subhorizontal axes (L_{S3}); ESE-/E-trending axial planes (S_{S3}); no evidence of anatexis *Below carapace* Absent	*In carapace (detachment zone)* S/S>L tectonites; steep-dipping mylonitic foliation (S_{G2}). ENE-/NE- and ESE-trending shear zones in north and south, respectively; gentle to moderately plunging stretching lineation (L_{G2}); sinistral, with south-down kinematics in S; opposite sense in north *Below carapace* As observed in carapace

Subscripts: N: anatectic gneiss; S: supracrustals; G: granitoids.

comprising highly sheared shallow-dipping rocks that range in thickness from a few meters to several kilometers, and (3) the unmetamorphosed/lower metamorphic grade rocks of the hanging-wall overlying the detachment zone. The identification of these features in the Precambrian crystalline rocks of the CGC is used in this study to propose a MCC structure for the area. Domains I and II represent the metamorphic core and detachment zone of the MCC, respectively. The striking difference in the metamorphic grade and structure of the granulite facies basement gneisses and the overlying amphibolite facies supracrustal rocks suggests that the supracrustal unit formed part of the hanging wall of the MCC and preserves deformation associated with the detachment zone formation. Unfortunately, due to extensive weathering and erosion, the only surviving remnants of the supracrustal unit are exposed in Domains III and IV. Although not included in conventional MCCs, steep-dipping shear zones are increasingly recognized as integral parts of MCC evolution [10, 38, 40–42, 45].

3.1. Domain I (the Core of the Complex). In the anatectic basement gneisses, the earliest recognizable planar fabrics are leucosome layers that are concordant with the pyroxene ±hornblende±biotite segregations (S_{N1}; D1 deformation; Table 1). Garnet is ubiquitous in both the leucosomes and the matrix. Coarse grains of orthopyroxene, clinopyroxene, and hornblende are common in the leucosomes in the felsic orthogneisses. The S_{N1} layers are typically isoclinally folded and are intrafolial to the pervasive gneissic layering (S_{N2}: D2 deformation; Table 1) in the basement gneisses, resembling metatexite layers. The folds on S_{N1} leucosomes are characterized by thickened hinges and strongly attenuated and commonly boudinaged limbs. The S_{N2} metatexite layering in the anatectic gneisses is steeply dipping (dip > 65°),
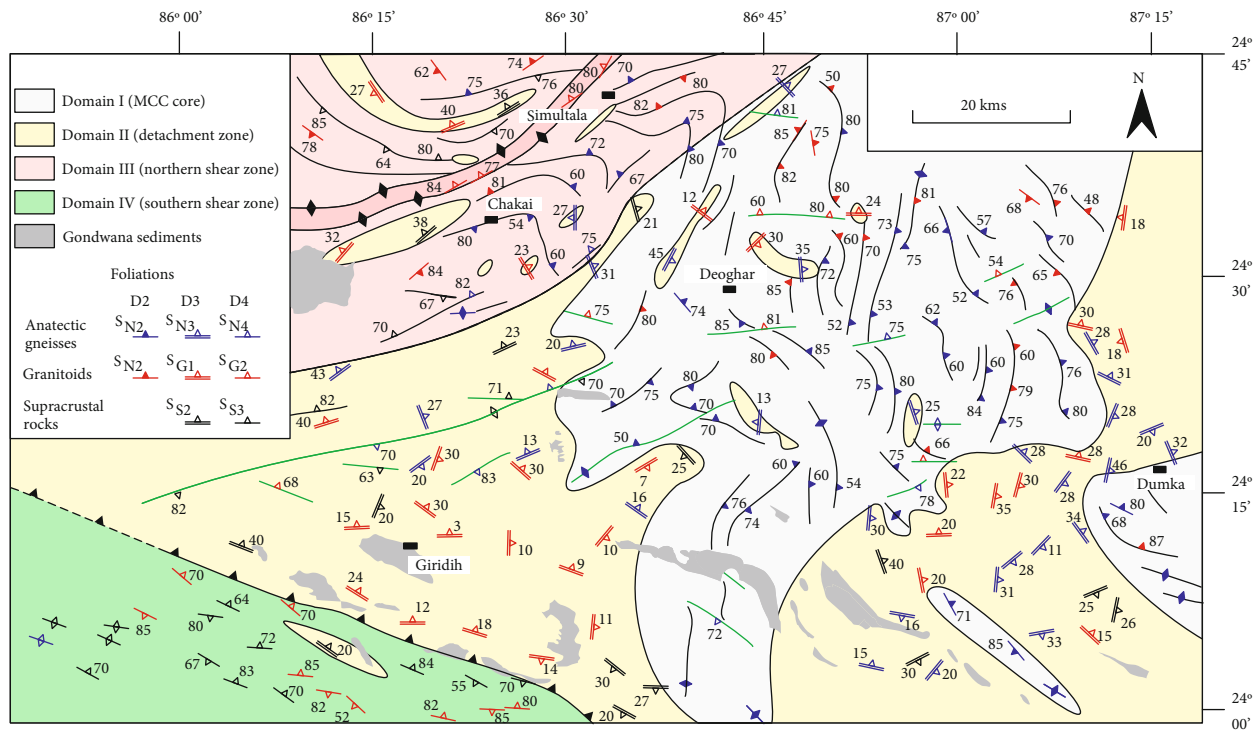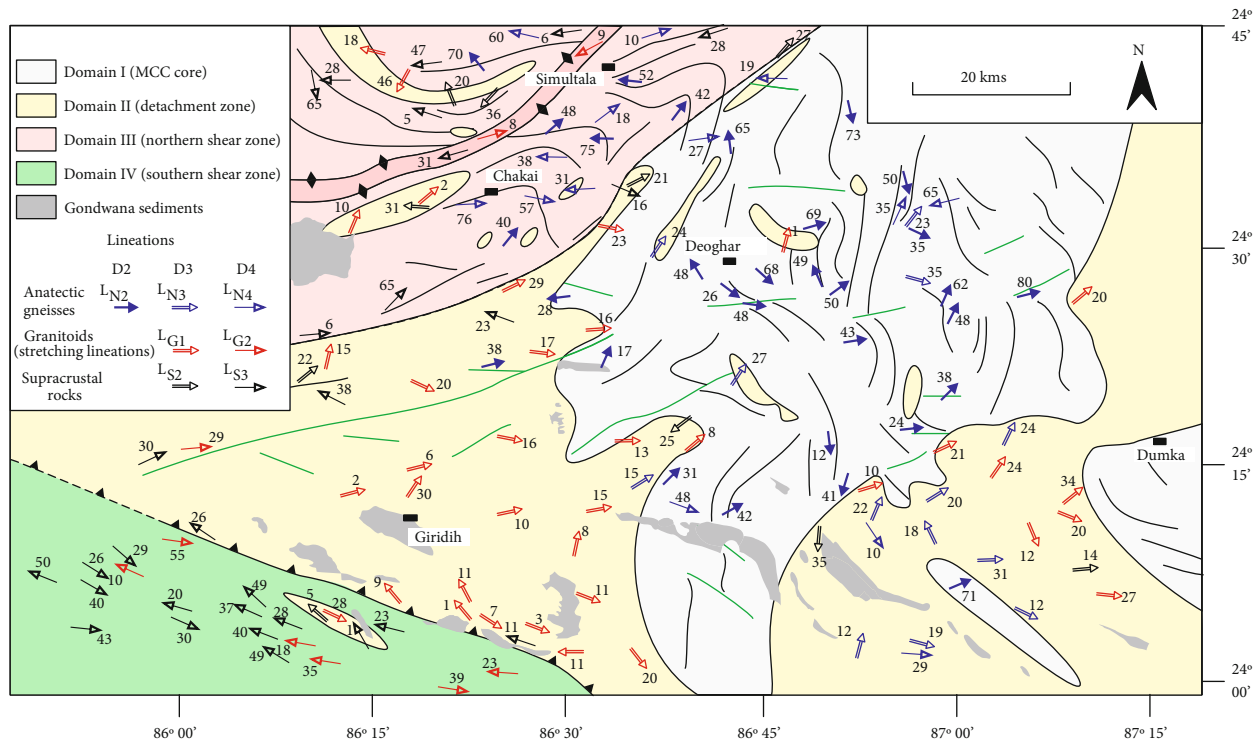
Figure 2: (a) Planar and (b) linear deformation structures in structural Domains I–IV in the Giridih-Dumka-Deoghar-Chakai area. Refer to text for details.

sinuous yet broadly N-trending in the east-central part of the area, and swings to NW through WNW to W in the NW (Figures 2(a) and 3(a)). The S_{N1}-S_{N2} layers in the gneisses are disrupted and/or truncated by coarser-grained syn-D2 diatexite pods typically 15–20 cm in diameter (also garnet ±pyroxene bearing) at the necks of pre-S_{N2} leucosome
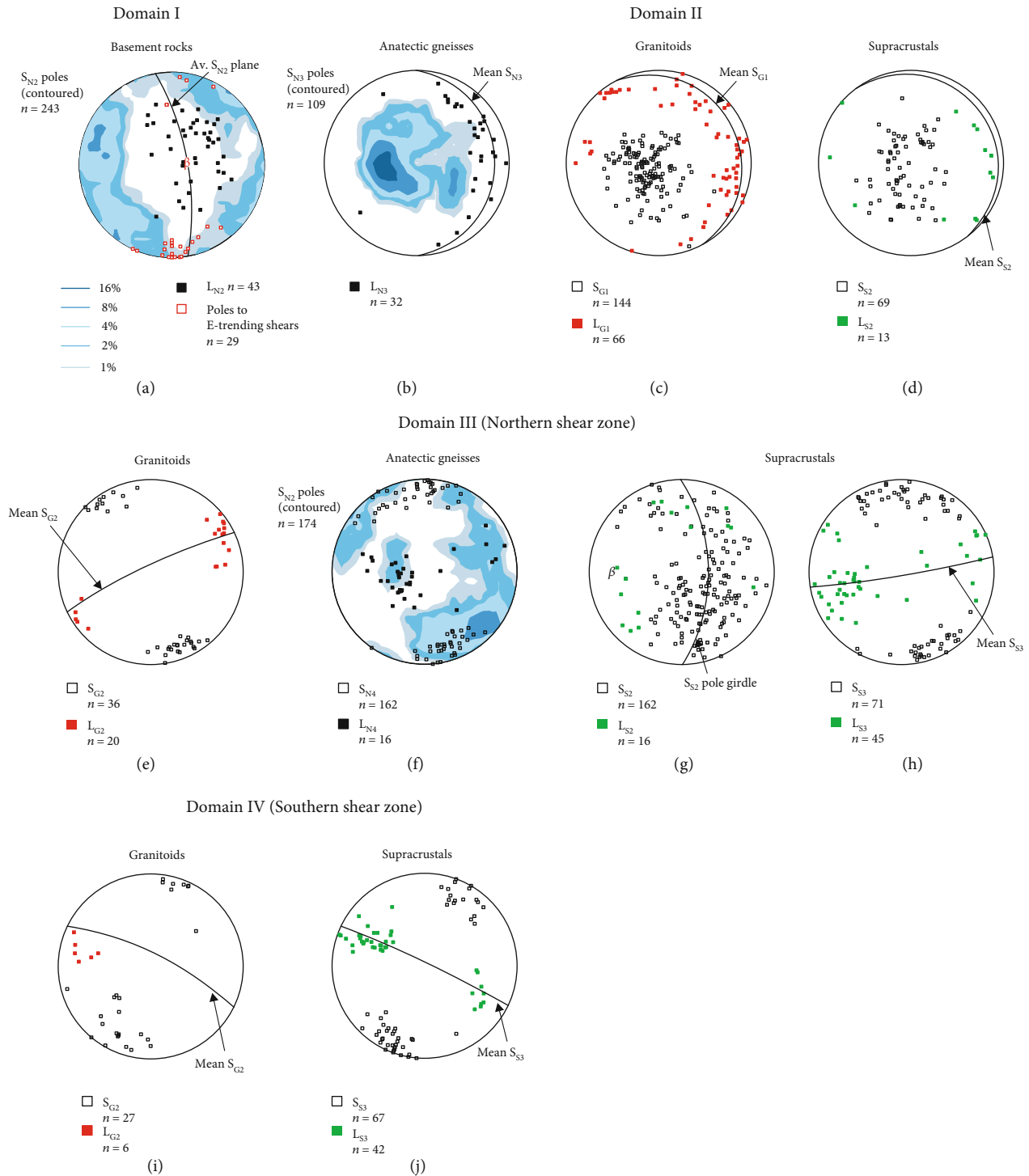
FIGURE 3: Lower hemisphere stereographic projections of planar and linear structures in Domains I to IV. Poles to foliation are shown by open squares, fold axes in gneisses by black squares and in supracrustals by green squares, and stretching lineations in granitoids shown in red squares (n = number of data). Domain I: (a) poles to the S_{N2} gneissic layering (contoured) and L_{N2} fold axes. Poles to E-trending D4 shears in the gneisses are also shown. Domain II: (b) poles to the shallow-dipping S_{N3} foliation in the anatectic gneisses and L_{N3} fold axes. (c) Poles to shallow dipping S_{G1} in granitoids with the associated L_{G1} stretching lineations. (d) Poles to shallow-dipping S_{S2} and L_{S2} fold axes. Domain III: (e) poles to S_{G2} foliation and L_{G2} stretching lineations in granitoids in the northern shear zone. (f) Poles to reoriented S_{N2} foliation (contoured) in anatectic gneisses, poles to axial planar S_{N4} foliation and L_{N4} fold axes. (g) Poles to folded S_{S2} foliation in supracrustal rocks with L_{S2} fold axes. (h) Poles to axial planar S_{S3} shear zone foliation in supracrustal rocks with L_{S3} fold axes. Domain IV: (i) poles to S_{G2} foliation in granitoids with L_{G2} stretching lineations. (j) Poles to S_{S3} foliation in supracrustal rocks and L_{S3} fold axes.
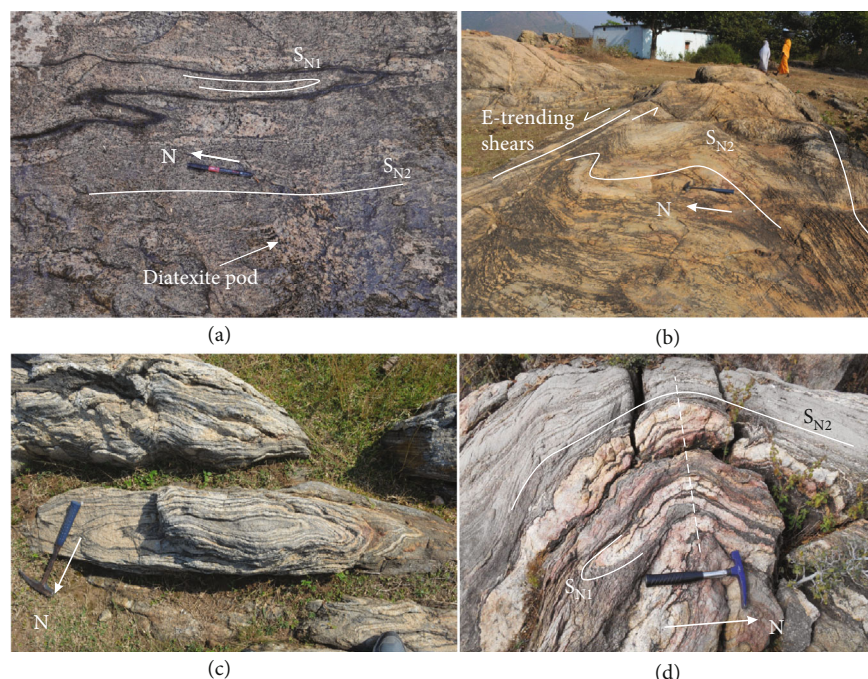
FIGURE 4: Field photographs of anatectic gneisses in Domain I. (a) Penetrative S_{N2} metatexite layers with syntectonic diatexite pods occurring at the boudin neck of S_{N1} leucosome layers. Note the D2 isoclinal folds on the S_{N1} layers (rimmed by biotite selvages) in the S_{N2} interfolial domains. (b) E-trending shears modify N-trending D2 gneiss layers. (c) Rare E-trending sheath folds. (d) E-trending hook-shaped superposition structure due D2 and D4 folds (axial plane of D4 folds in broken line) on the S_{N1}/S_{N2} layers.

boudins (Figure 4(a)). These diatexite melt pods comprise a small fraction (<10 area %) of the rock in any outcrop.

The basement gneisses were intruded by granitoids in two stages. The structurally older granitoids share the S_{N2} fabric in the gneisses but do not contain the intrafolial folded leucosome layers (S_{N1}) and are thus post-D_1 but pre-D_2. The fabric within these granitoids is defined by schlieren of ferromagnesian phases (biotite, hornblende, and pyroxene), quartz ribbons, and drawn-out aggregates of dynamically recrystallized feldspars. A suite of granitoids that lack mesoscale fabrics cross-cut the S_{N2} fabric in the gneisses and are thus inferred to be post-D_2 intrusives.

The outcrop and regional scale sinuosity in the S_{N2} layers in the gneisses and the variations in L_{N2} fold axes (estimated from the S_{N1}-S_{N2} intersection lineations) are related to folding induced by locally penetrative discontinuous subvertical E-/ENE-/WNW-trending shears (Figures 2(a) and 4(b)). These shear zones are possibly genetically related to the steep-dipping shear zones in Domains III and IV (D4, Table 1, discussed later). The steeply plunging β-axis obtained from the S_{N2} pole girdle in Domain I (Figure 3(a)) suggests that the shear-related fold axes are steeply inclined to recline in the regional scale. Sheath folds are locally observed (Figure 4(c)) in these E-trending shear zones. These shears produce a locally penetrative fabric in the post-D_2 granitoids wherever affected, but melting was not synchronous with shearing. The field features taken together demonstrate that pre-D_2 melt productivity (vol% melt) during high-grade metamorphism in the basement gneisses waned considerably during D_2, and leucosome formation in the base-

ment gneisses did not occur during the development of the E-trending shears.

The structural context of the samples with U-Pb age determinations [67–69] is lacking (see later), and this complicates attempts to infer the age of formation of N-striking steeply inclined D1-D2 fabrics in the Dumka-Deoghar area. Since the lithologies discussed by Mukherjee and coworkers possess at least one penetrative gneissic fabric which is N-striking (cf. [67]), it appears that the D1-D2 composite fabric formation and associated high-grade metamorphism and felsic magmatism in Domain I may have occurred between 1.46 and 1.6 Ga.

3.2. Domain II (the Detachment Zone). All three lithodemic units in Domain II exhibit a shallow-dipping foliation. D1-D2 fabrics in the screens of basement gneisses interleaved with granitoid mylonites in this domain exhibit recumbent to gently inclined folds (D3; Table 1); however, axial planar fabrics (S_{N3}) corresponding to these folds (Figure 3(b)) are absent or only locally developed (Figures 5(a) and 5(b)). These recumbent folds affect the anatectic gneisses only at structurally higher levels in the crust; at deeper levels, the unmodified D_1-D_2 fabrics are steep dipping (cf. [62]). The D3 deformation is 0.9–1.1 Ga (see section on monazite dating), limited to a carapace over the basement. The basement remains largely unaffected by this deformation, as expected for the detachment zone formation in an MCC. In close-spaced outcrops, the axial planes (S_{N3}) of the recumbent/gently inclined folds in the gneisses are broadly coplanar with the shallow-dipping mylonite foliation (S_{G1}) in the
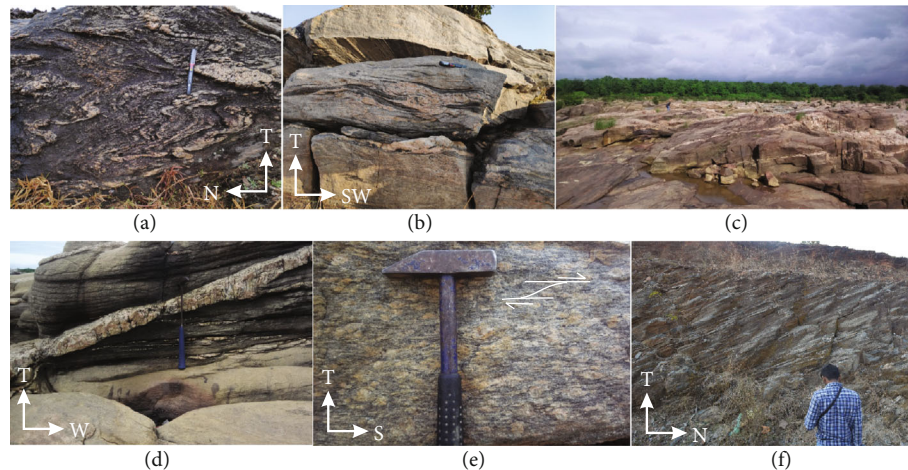
FIGURE 5: Field photographs of shallow-dipping/flat-lying structures in Domain II. (a) Shallow-dipping anatectic gneisses. Note the interfolial recumbent folds on the anatectic layers. (b) Recumbent folds (looking east) defined by leucocratic layers in anatectic gneiss. (c, d) Extensive flat-lying granitoid mylonites in the Usri riverbed. (d) Close-up view of the granitoid mylonites in (c). (e) K-feldspar porphyroclasts in granitoid mylonites showing top-to-the-south kinematics in the Y-Z section perpendicular to stretching lineation and foliation. (f) Shallow-dipping foliation in amphibolites in the supracrustal unit.

granitoids (Figures 3(b) and 3(c)). The L_{N3} fold axes of the gently inclined folds in the gneisses straddle the mean S_{N3} axial plane (Figure 3(b)).

Domain II is dominated by shallow-dipping granitoid mylonites best described as S and S>L tectonites (Figures 5(c) and 5(d)). The shallow-dipping mylonitic foliation (S_{G1}; D3 deformation, Table 1) in the basement granitoids generally dips northwards, with S-dipping planes more common in the south (Figures 2(a) and 3(c)). The regionally warped foliation is monophase in the majority of the granitoids; the pre-D_2 granitoids, however, show rare recumbent folds on the former layering in the intrafolial domains of the penetrative S_{G1} foliation. Stretching lineations (L_{G1}) are uncommon in the shallow-dipping granitoid mylonites, possibly due to intense dynamic recrystallization accommodating size reduction in the feldspar clasts.

At a regional scale, the orientations of L_{G1} straddling the mean S_{G1} plane (Figure 3(c)) are similar to the L_{N3} fold axes in the anatectic gneisses (Figure 3(b)). Mesoscale S-C fabrics are rare within these rocks, and asymmetry in feldspar clasts is observed only in few outcrops (Figure 5(e)). As a result of the lack of stretching lineations and mesoscale shear sense indicators in the shallow-dipping granitoids (D3), the kinematics of shearing associated with the formation of the detachment zone could not be ascertained. In a few outcrops, top-to-the-north kinematics in sections parallel to lineation and perpendicular to foliation (X-Z sections of strain ellipsoid) is inferred from S-C fabrics and asymmetry of feldspar clasts in the northern parts of the domain. In S>L tectonites, in the southern parts of Domain II, top-to-the-south kinematics is inferred (Figure 5(e)).

The supracrustal rocks in Domain II exhibit a shallowly dipping penetrative schistosity (S_{S2}; Figure 5(f)) broadly coplanar with the shallow-dipping S_{N3} and S_{G1} fabrics in the anatectic gneisses and granitoids, respectively (Figure 3(d)). This penetrative S_{S2} schistosity in the mica schists (quartz, biotite≥muscovite, ilmenite±garnet±sillimanite (altered to pyrophyllite)±plagioclase) within the supracrustal unit is a crenulation cleavage (D3 deformation, Table 1); the pre-S_{S2} fabrics, largely obliterated, occur as oblique strands and relic hinges of microfolds on muscovite-biotite aggregates in the S_{S2} intrafolial domains. In amphibolites associated with the mica schists, both the former and the S_{S2} fabrics are defined by aggregates of hornblende±epidote in a polygonized mosaic of plagioclase-quartz. In Domain II, the S_{S2} foliation is commonly crenulated possibly due to the D4 deformation, especially approaching the flanking Domains III and IV (Figure 6(a)). Garnet porphyroblasts, uncommon in the mica schists, overgrow the S_{S2} schistosity (Figures 6(a) and 6(b)). We tentatively infer the garnets to be post-S_{S2}, although garnet-hosted inclusion trails are lacking, and therefore, S_i-S_e relations critical for establishing garnet growth in relation to the external fabric could not be unequivocally ascertained. The garnet porphyroblasts hosted in the shear zones are pretectonic with respect to S_{S3}, D4 deformation (Figure 6(c)).

3.3. Domains III and IV (the Steeply Dipping Shear Zones). Domain III encompasses the ENE-trending shear zone (Figures 2 and 7(a)–7(c)) in the north and the structures neighboring it, while Domain IV constitutes an ESE-trending shear zone (Figures 2 and 7(d)–7(f)) in the south. The formation of these basement-penetrative shear zones represents the final deformation event (D4), which is also Early Neoproterozoic in age (see later). Proximal to Domains III and IV, the shallowly dipping D3 fabrics in the detachment zone exhibit open to close and upright to steeply inclined E-/ESE-trending D4 folds with gently plunging axes. The long limbs of the asymmetric folds are north-dipping in Domain III (Figure 7(c)) and south-dipping in Domain IV. By contrast, D4 folds on steeply dipping S_{N2} fabric in the basement gneisses below the detachment zone—unaffected by D3 recumbent folding—exhibit steeply dipping E-/ESE-trending axial planes (S_{N4}) with steeply plunging fold axis L_{N4} (Figures 3(f) and 4(d)).
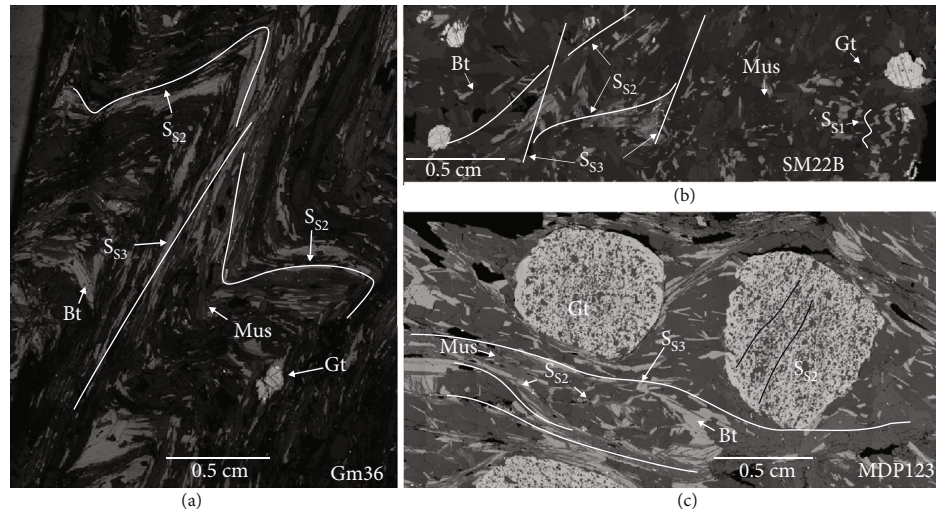
FIGURE 6: Back-scatter electron (BSE) images of paragenetic relations of garnet in mica schists. (a, b) Crenulated S_{S2} schistosity (in Domain II) truncated by locally developed S_{S3} schistosity. Note the post-S_{S2} garnet porphyroblasts. (c) Garnet porphyroblasts studded with S_{S2} mineral inclusion trails wrapped by penetrative S_{S3} schistosity in the southern shear zone.
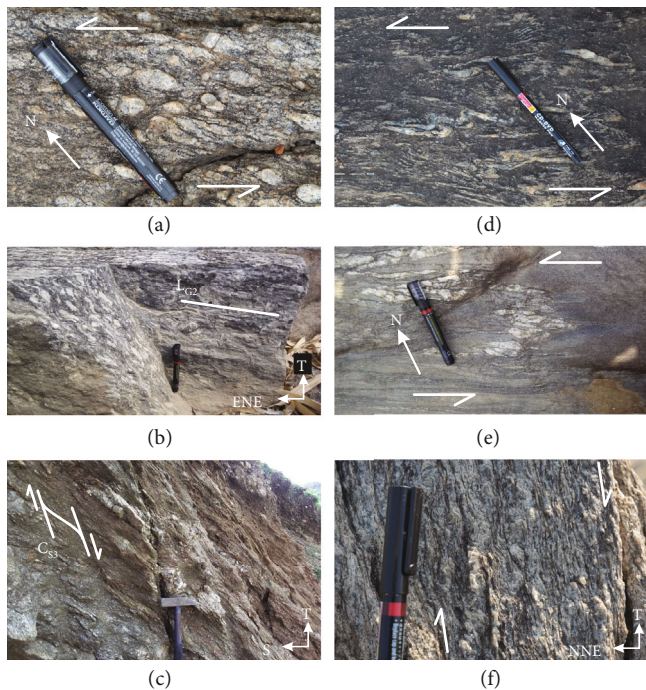

FIGURE 7: Field photographs of mesoscale structures in the northern (a–c) and the southern (d–f) shear zones. Northern shear zone: (a) Feldspar clast asymmetry showing sinistral kinematics (plan view), (b) subhorizontal stretching lineation in ESE-trending steep-dipping granitoid mylonite, and (c) C_{S3} shear bands in the Y-Z section showing north-down kinematics in mica schists. Southern shear zone: (d) sinistral kinematics exhibited by sigmoid quartz veins and the S-C relationship in schists (plan view) and (e) sinistral sense of shearing exhibited by quartz ribbons at the shredded hinges of quartzite bands in mica schist (plan view). (f) Asymmetric feldspar clasts in granitoid protomylonite showing south-down kinematics in the Y-Z section (looking ESE).

S and S>L tectonite granitoids within both shear zones are steeply dipping mylonites (S_{G2} foliation), with stretching lineations defined by drawn out K-feldspar clasts and stretched quartz ribbons oriented subhorizontally in the north (L_{G2}; Figures 3(e) and 7(b)) and moderately plunging in the south (L_{G2}; Figure 3(i)). Porphyroclast-matrix relations indicate that both the northern (Figure 7(a)) and the southern shear zones (Figures 7(d) and 7(e)) record a sinistral shear sense on horizontal surfaces (approximating the X-Z section of the strain ellipsoid). In vertical sections oriented perpendicular to the mylonite foliation and stretching lineation (i.e., the Y-Z section of the strain ellipsoid), asymmetry in feldspar clasts is less prominent; however, north-down kinematics are inferred for the Domain III northern shear zone (Figure 7(c)) and south-down motion in the Domain IV southern shear zone (Figure 7(f)). In high-strain domains within the ENE-trending northern shear zone, a set of SE-trending C" shear bands with dextral kinematics is persistently developed.

As the two flanking shear zones are approached, subhorizontal to moderately plunging asymmetric folds (D4 deformation, Table 1) are developed on the shallow-dipping gneisses (S_{N3}) and supracrustal rocks (S_{S2}) in the detachment zone. These features become progressively more tightly folded (Figure 3(g)) within the shear zones, where the S_{S2} schistosity is ultimately transposed to S_{S3} schistosity (Figures 3(h) and 3(j)). Locally, however, the shallowly dipping supracrustal rocks, albeit crenulated, occur as lens-shaped rafts of low D_{S3} strain within the shear zones (Figure 2). Synthetic C_{S3} shear bands (Figure 7(c)) exhibit sinistral and north-down kinematics in Domain III and sinistral and south-down sense of movement in Domain IV.

The northern and southern shear zones appear to converge in the west of Giridih (Figure 1(b)), but no coherent analysis could be made about the temporal relationship between the two sinistral shear zones. However, because of the overlapping monazite ages (see later), these two shear zones are interpreted to be synchronous and formed during the same D4 deformation event.

4. Crystallographic Analysis

Crystallographic fabrics from plastically strained rocks reflect the kinematics of deformation. To better understand the structural evolution of the CGC, we collected crystallographic data from six samples, two each from Domains II, III, and IV. Polished thin sections of samples oriented perpendicular to foliation and parallel to lineation were analyzed using electron back-scatter diffraction (EBSD) at Washington and Lee University. The data were collected with an Oxford EBSD with Aztec software on a Zeiss EVO-MA 15 SEM. To avoid charging, analyses were conducted in variable pressure mode with a chamber pressure of 30 Pa. Machine conditions included an accelerating voltage of 25 kV, a probe current of 20 nA, and a working distance between 24 and 28 mm. Data were collected on a rectangular grid with a spacing between 12 and 30 μm (chosen based on sample grain size); observations from a series of 500 μm × 375 μm scan regions were montaged into a single map within Aztec for analysis. Scan areas ranged from 175 to 300 mm^2. The crystallographic data were processed using v. 5.1.1 of the MTEX toolbox [76].

Crystallographic fabrics are generally viewed in a reference frame defined by the foliation and lineation. In many cases (e.g., simple shear), the vorticity axis of a deformation is oriented perpendicular to lineation within the foliation plane, so this reference frame is best for interpreting the deformation kinematics. However, in some situations (e.g., transpression), the vorticity axis may be aligned parallel or oblique to lineation [77]. Since the D3-D4 deformations involve transpression (see later), we apply crystallographic vorticity axis (CVA) analysis to determine an appropriate reference frame to view the crystallographic data [78]. In this technique, the dispersion of crystallographic orientations within each grain is used to determine the vorticity axis for that crystal. The average of many individual observations is interpreted to represent the vorticity axis for the bulk deformation.

We utilized an MTEX algorithm developed by Michels et al. [78] to perform a CVA analysis for each sample. For four of our six samples, the estimated vorticity axis is positioned nearly perpendicular to the lineation and within the foliation plane (i.e., as would be expected for a monoclinic deformation). However, for two of the samples: GM 2 (Domain II) and GM 57 (Domain IV), the calculated vorticity axis is within the foliation plane but oblique to the lineation. This is a characteristic of triclinic deformation [79, 80]. Misalignment of the quartz CPO patterns with the lineation/foliation reference frame has been observed previously (e.g., [81–83]). In these studies, the crystallographic data are rotated around the pole to foliation until a conventional quartz CPO pattern is observed. Rather than apply an arbitrary rotation, we achieve a similar effect by instead rotating the data to place the CVA in the center of the pole figure.

4.1. Domain II.
The CVA analysis for GM 2 reveals a vorticity axis within the foliation plane but oblique to the lineation, indicative of a triclinic deformation. Rotation of these data to place the vorticity axis in the center of the pole figure produces a c-axis fabric (Figure 8(a)), albeit one that is diffi-

cult to interpret. Most prominent is a strong girdle stretching from the bottom to top of the pole figure; additionally, two poorly defined limbs are oriented within the foliation plane (along the left-to-right axis in the pole figure), giving an appearance reminiscent of a cross-girdle. If this is a cross-girdle, it has an unusual orientation, since cross-girdle limbs generally split around the pole to foliation [84]. Alternatively, the fabric may represent a poorly defined single girdle, with the subordinate limbs observed in the foliation plane corresponding to noise.

In contrast to GM 2, the c-axis pattern for GM 24 is poorly defined. We attribute the lack of a strong fabric, at least in part, to an insufficiently large sample. Although data were collected from an area > 175 mm^2, the large grain size (500-2200 μm) (Figure 8(b)) limited the number of grains in the analysis and prevented us from defining a clear c-axis fabric. Nevertheless, sample GM 24 does show a preferred orientation in the positive and negative rhombs (r and z). For instance, the z orientation lacks orientations parallel to the vorticity axis (center of pole figure) as well as along the upper left and lower right margins of the pole figure. Both experimental [85] and observational [86–88] studies have shown that rhomb-dominated fabrics may develop even in the absence of strong c-axis fabrics. This pattern reflects Dauphiné twinning (a 60° rotation around the quartz crystallographic c-axis) triggered by a response to stress. Because the elastic modulus of quartz varies with crystallographic direction, crystals loaded against the relatively inelastic z face will twin to bring the more compliant r-face towards the compression axis. In noncoaxial shear zones, the instantaneous shortening direction is perpendicular to the vorticity axis and inclined with respect to the foliation plane. The preferred orientations of the rhombs (Figure 8(b)) are therefore consistent with dextral shear (top-to-the-ESE), in which shortening on an axis from the upper left to lower right of the pole figure triggered Dauphiné twinning that created the observed void in z-faces in that direction.

4.2. Domains III and IV.
Four samples, two from each of the steeply dipping, high-strain shear zones that bound the complex, were analyzed. The samples from Domain III (the northern shear zone) show patterns reminiscent of sample GM 24. Both samples lack an obvious c-axis fabric, a fact we again attribute at least in part to the relatively large grain size of these samples. GM 75 (Figure 8(c)) displays a preferred orientation within the rhombs in a nearly identical fashion to GM 24; accordingly, we infer that this sample may have been affected by dextral shear. Although GM 76 also displays a similar pattern in the rhombs (Figure 8(d)), in this case, the z-rhomb maxima are oriented perpendicular to the foliation and parallel to the lineation. Tentatively, we suggest that this pattern indicates a greater contribution of pure shear deformation.

Like sample GM 2, CVA analysis for GM 57 demonstrates a vorticity axis oblique to the sample lineation. Centering the data on the vorticity axis reveals a typical type I cross-girdle (Figure 8(e); [89]) suggesting a significant pure shear component to the deformation. This type of fabric is amenable to quartz opening angle thermometry, an empirical
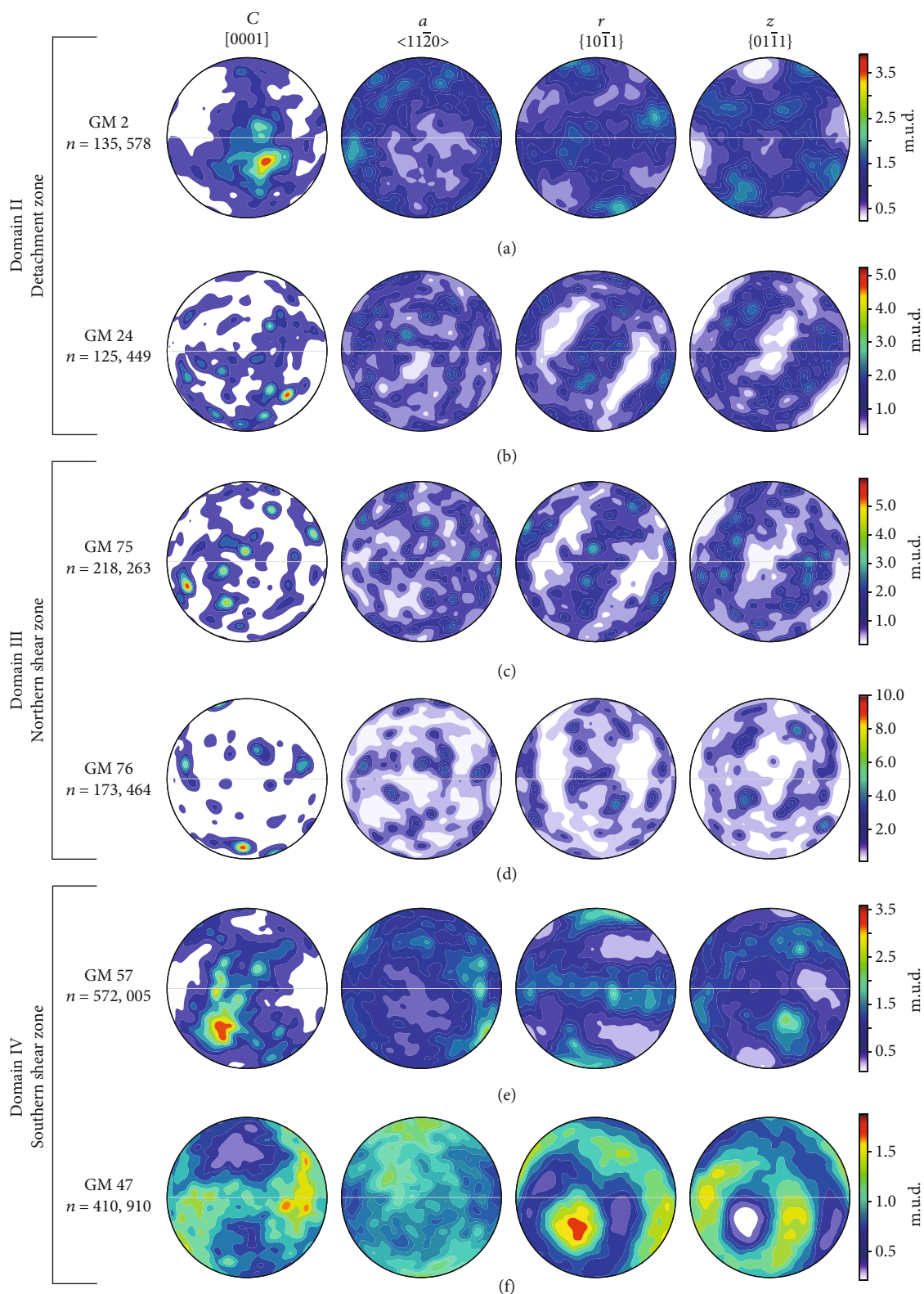
FIGURE 8: Lower hemisphere pole figures of contoured quartz crystallographic data. All data from each sample are included; pole figures contoured based on one-point-per-grain (not shown) look similar. Except for samples GM 2 and GM 57, the figures are oriented with the pole to foliation on the N-S axis and the lineation oriented E-W. Data for GM 2 and GM 57 have been rotated to position the vorticity axis determined from the CVA analysis in the center of the pole figure. In these cases, the N-S axis remains approximately normal to the foliation. Orientations are shown for the <[0001]> (c-axis), <11–20> (a-axis), {10–11} (positive rhomb, r), and {01–11} (negative rhomb, z) directions. n: number of observations; m.u.d.: multiples of uniform density. Sample locations are shown in Figure 1(b).

approach based on the observation that quartz opening angles increase with deformation temperature [90, 91]. We quantified the opening angle for GM 57 using an MTEX routine that quantifies fabric intensities around the perimeter of a pole figure [92]. The measured opening angle of 80° indicates a temperature of ~600°C using the calibration of Faleiros et al. [93].

Sample GM 47 shows an exceedingly weak crystallographic fabric (Figure 8(f)), with c-axis maxima no more than 1.8 times uniform distribution. Unlike for samples GM 24, 75, and 76, a large area was scanned relative to the grain size (median of ~100 μm from the EBSD dataset), and we regard the random fabric as real rather than a small-sample artifact. The lack of a quartz CPO suggests an important role for a mechanism other than dislocation creep. The small grain size suggests an important role for grain boundary sliding [94]. Numerous studies have shown that grain size reduction during recrystallization can cause a transition to diffusion creep and associated grain boundary sliding that can weaken and randomize an existing CPO (e.g., [95–97]). Experimental work suggests that very high shear strains, on the order of $\gamma > 17$, are required to disaggregate mineralogic layering and generate well-mixed ultramylonites that lack a CPO [98]. The anticorrelation between the positive and negative rhombs is again interpreted to reflect stress-induced Dauphiné twinning.

5. Kinematic Vorticity Analyses Using Rigid Clasts

Kinematic vorticity estimates provide a measure of the contribution of pure shear ($W_k = 0$) and simple shear ($W_k = 1$) during deformation [99]. Fossen and Tikoff [100] consider equal contributions of pure shear and simple shear at $W_k = 0.81$, whereas Law et al. [101] consider the value to be $W_k = 0.71$ for shear zones with monoclinic symmetry. Vorticity estimation from rotation of rigid porphyroclasts assumes steady-state deformation and monoclinic symmetry with the VNS (vorticity normal section) parallel to the XZ section in the rock [102]. Although CVA analysis indicates that some samples record triclinic deformation, many samples exhibit monoclinic symmetry. We therefore applied the porphyroclast aspect ratio (PAR; [103]) method to measure the mean vorticity number (Wm; [102]) for three granitoid mylonites in Domain III and one sample from Domain II to better estimate the kinematics of formation of the steep-dipping shear zones (D4) and the detachment zone (D3).

The PAR method estimates the mean kinematic vorticity number (Wm) by plotting the aspect ratio ($R =$ long axis/short axis) of rotated rigid clasts against φ, the angle between the long axis of the clast and the flow plane (taken as the foliation plane in our study) [102]. The rock matrix is assumed to behave like a Newtonian linear-viscous fluid with freely rotating rigid porphyroclasts perfectly bonded with the matrix [102]. The plot is divided into two fields by the critical aspect ratio (R_c) which separates the clasts that rotated continuously, from the clasts that obtained stable sink orientations. The R_c value is then

used in the equation $Wm = (R_c{}^2 - 1)/(R_c{}^2 + 1)$ [104] to calculate the mean vorticity number associated with the deformation. Although vorticity estimates using rigid porphyroclasts are widely used, the results may have large uncertainties [105, 106].

A mylonitic granitoid sample (Figure 5(e)) from the detachment zone (Domain II) containing a well-developed N-trending stretching lineation with the size of the long axis of the clasts varying from a couple of mm to more than 2 cm in diameter was chosen. Kinematic analyses should be performed on the vorticity normal section (VNS), identified as the plane of maximum asymmetry perpendicular to the foliation plane. Several sections at varying angles from the strike were cut to determine the VNS (cf. [107, 108]) in the Domain II sample but no perceptible difference in asymmetry was observed. However, R_c estimations were made in three sections cut normal to the foliation (Figures 9(a)–9(c)): (a) parallel to the lineation (XZ section), (b) perpendicular to the lineation (YZ section), and (c) 45° from the lineation. The clast measurements made on photographs of polished slabs yielded overlapping ranges of R_c values that translate to Wm values 0.59–0.74. Taken simply, these values indicate that the deformation was marginally dominated by pure shear.

Vorticity estimations for the shear zone forming D4 deformation were obtained from three steep-dipping granitoid mylonites with a subhorizontal stretching lineation and well-defined clasts from the northern shear zone (Figure 7(b)). After making several sections perpendicular to foliation, the maximum asymmetry displaying sinistral shear sense was observed in sections close to the horizontal surface (XZ section). This confirms that the northern shear zone approximates a monoclinic symmetry, consistent with the crystallographic analysis discussed above. The Wm estimates (Figures 9(d)–9(f)) in the three samples are comparable, ranging between 0.60 and 0.74, with an average value of Wm = 0.67, indicating a marginally larger component of a pure shear than a simple shear associated with the deformation.

6. Metamorphic P-T Conditions in the Supracrustal Unit

The metamorphic P-T evolutionary history of supracrustal rocks has been reconstructed along the southern accretion zone the CGC shares with the Singhbhum Craton [73, 74]. However the P-T path of the supracrustal rocks in the central part of the CGC distal from the accretion is unknown. One of the reasons for the lack of detailed P-T work stems from the fact that key minerals in these rocks have been altered due to intense weathering (garnet especially is commonly replaced by martite, and sillimanite is altered and replaced by pyrophyllite). Here, we provide a new P-T path evolutionary history retrieved from a muscovite-biotite mica schist (SM-22B; Figure 10) consisting of garnet, sillimanite, and minor amounts of chlorite, plagioclase, and ilmenite. The sample is located in Domain II, but close to the boundary with Domain III (Figure 1(b)).
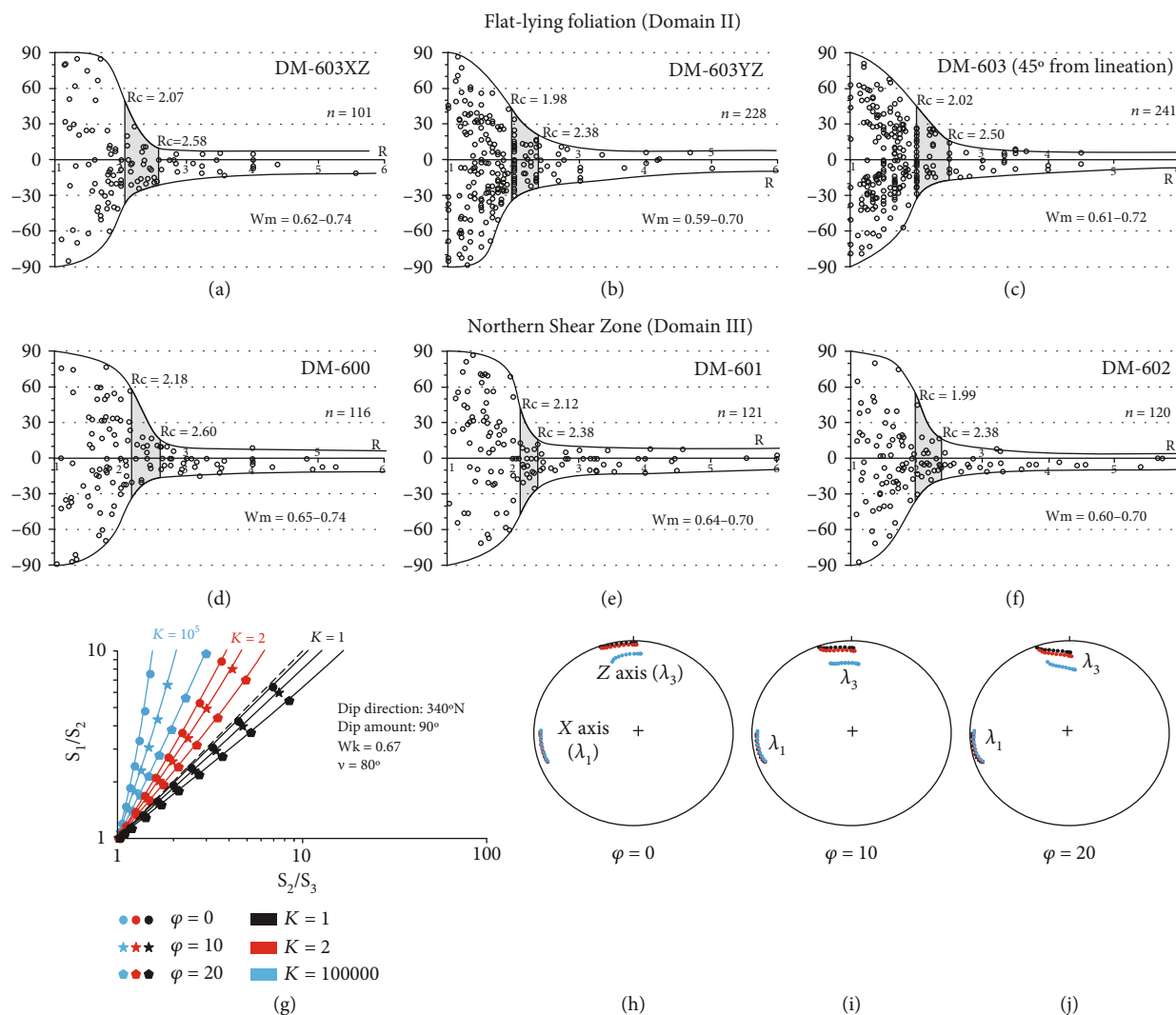
FIGURE 9: (a–f) Kinematic vorticity (Wm) values obtained from the porphyroclast-matrix relation using the PAR method [103]. XZ section (a), YZ section (b), and section 45° from lineation (c) in a Domain II sample. (d–f) X-Z sections in three samples from Domain III. Sample locations shown in Figure 1(b). (g–j) Results of kinematic modeling following Fernandez and Diaz-Azpiroz [155] for the northern shear zone. Average Wm value Wm = 0.67 is used for modeling. (g) Logarithmic Flinn diagram showing the shape of the finite strain ellipsoids for different parameters chosen. (h–j) Equal-area lower hemisphere projections of variation of the maximum (λ_1) and minimum (λ_3) principle quadratic extensions (finite deformation) are shown for different values of obliquity angle (φ).

The mica schist exhibits spaced muscovite-biotite-defined S_{S3} disjunctive cleavage axial planar to D4 crenulations on muscovite-biotite-sillimanite-defined S_{S2} schistosity. Chlorite replacing biotite randomly overgrows the S_{S3} crenulations. Garnet porphyroblasts truncate the S_{S2} mica-sillimanite aggregates in the S_{S3} interfolial domains but are pretectonic with respect to S_{S3} (Figure 6(c)). No post-S_{S3} sillimanite was observed. Two garnet porphyroblasts were examined in detail (Figures 10(a) and 10(b)). The margins of garnet grains are straight and not corroded (Figures 10(a) and 10(b)). In Figure 10(a) (bottom left), the garnet appears to mimic the shape-preferred aggregates of muscovite (±biotite). There is no evidence to suggest that the garnets were resorbed via retrograde reaction involving biotite/chlorite (Figures 10(a) and 10(b)). The profiles for the two garnet porphyroblasts (Figures 10(c) and 10(d)) are chosen so that the garnet rims

are juxtaposed with muscovite and not biotite. This ensures that the postgrowth chemical modifications in garnet composition due to Fe-Mg diffusive exchanges are minimal across garnet-biotite interfaces. In other words, the profiles indicate garnet growth. The core compositions of the garnets are $Py_8Alm_{86}Grs_3Sps_3$ and $Py_8Alm_{85}Grs_4Sps_3$, and the corresponding rim compositions are $Py_7Alm_{86}Grs_5Sps_1$ and $Py_7Alm_{85}Grs_6Sps_2$, respectively. The garnets are, for the most part, chemically homogenous (Figures 10(c) and 10(d)) but exhibit an increase in X_{Ca} (=Ca/(Mg+Fe+Ca)) and a decrease in X_{Mn} (=Mn/(Mg+Fe+Ca+Mn)) towards the rim. X_{Fe}' (=Fe/Fe+Mg) and X_{Fe} (=Fe/(Fe+Mg+Ca+Mn)) show a gentle rimward increase (Figures 10(e) and 10(f)).

The bulk composition of the mica schist (Figures 10(g) and 10(h)) is approximated to the system $MnO–Na_2O–CaO–K_2O–FeO–MgO–Al_2O_3–SiO_2–TiO_2–H_2O$

(a)

(b)

(c)

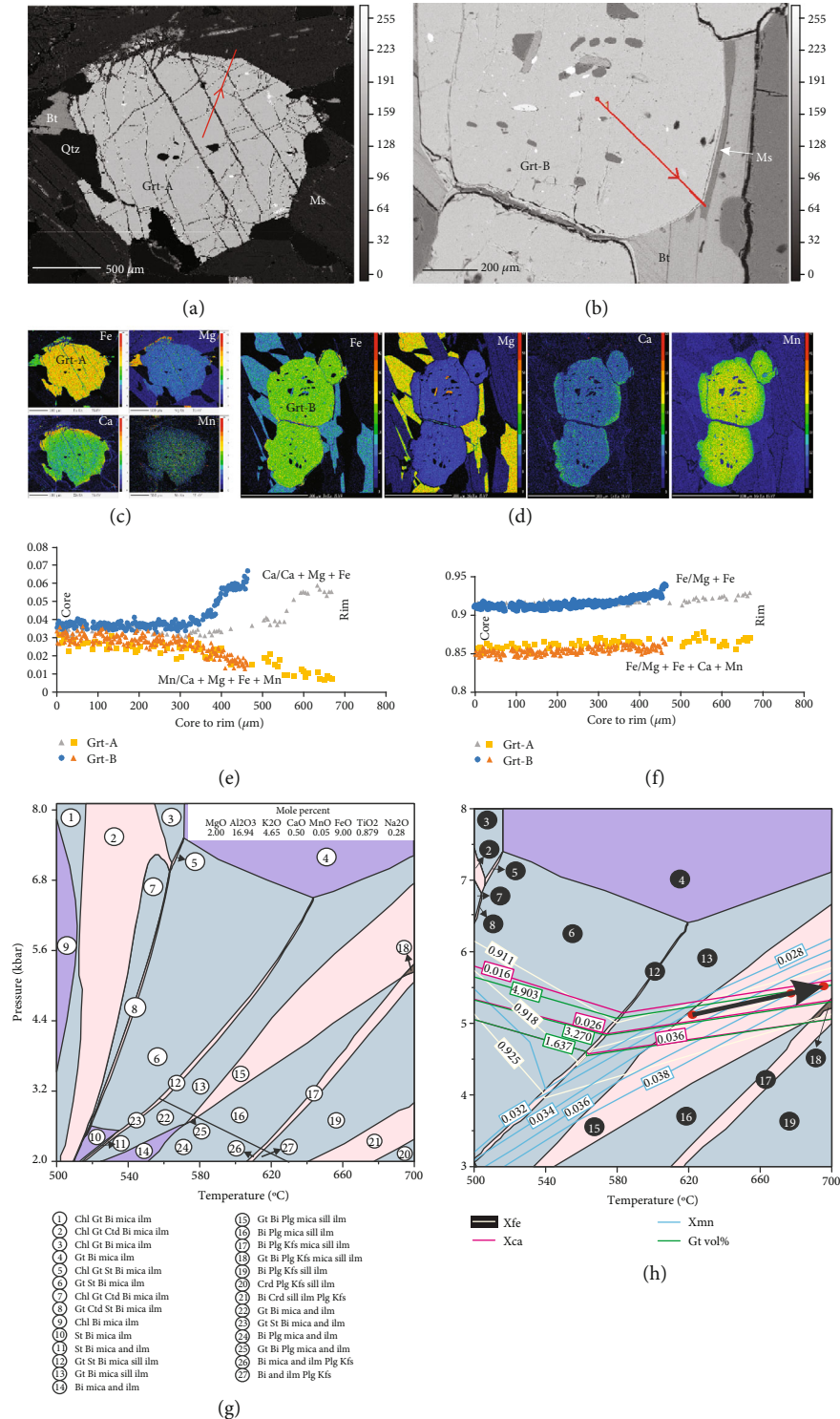(d)

(e)

(f)

(g)

(h)

FIGURE 10: Results of the P-T pseudosection analysis in mica schist (SM-22B). (a, b) BSE images of two garnets (labeled A and B) chosen for analysis. The profile lengths (shown in red line with arrow) and step sizes of analyses in the two garnets are 681 μm and 5.7 μm, and 471 μm and 2.0 μm for garnet-A and garnet-B, respectively. (c, d) Fe, Mg, Ca, and Mn X-ray element maps of the two post-S_{S2} garnets A and B. (e, f) Core to rim variations in X_{Ca} and X_{Mn} (e) and X_{Fe} and $X_{Fe'}$ (f) in the two garnets. (g) MnNCKFMASHT P-T pseudosection in SM-22B. (h) Blown up part of the same pseudosection. Bulk composition of SM-22B in mol% is shown in box. Bold black line with arrow in (h) is the P-T path for post-S_{S2} garnet stabilization in SM-22B. The bulk composition of the rock (analyzed using ICP-AES) in terms of major element oxides in wt% are the following: SiO_2 = 67.75, TiO_2 = 0.70, Al_2O_3 = 17.30, FeO = 6.40, MnO = 0.04, MgO = 0.80, CaO = 0.28, Na_2O = 0.25, K_2O = 4.38, H_2O (loss on ignition) = 1.10, and total = 99.05. Since silica is in excess, SiO_2 is not considered for computing the P-T pseudosection.

(MnNCKFMASHT). Fe_2O_3 contents in ilmenite are negligible. The MnNCKFMASHT P-T pseudosection for the sample was constructed using Perple_X_6.8.3 software [109] and the updated version of the internally consistent thermodynamic dataset of Holland and Powell [110].

The following phases and the phase components (in square brackets) were chosen from those listed in the software: garnet (Gt) [alm, py, gr, and sps], chloritoid (Ctd) [fctd, mctd, and mnctd], staurolite (St) [fst, mst, and mnst], Crd [crd, fcrd, hcrd, and mncrd], biotite (Bio) [ann, phl, east, and mnbi], chlorite (Chl) [ames, clin, daph, and mnchl], and muscovite (Mica) [mu, pa, cel, and fcel]. For both K-feldspar and plagioclase, the ternary feldspar (abh, an, and san) model was adopted. Clinozoisite (cz), zoisite (zo), andalusite (and), sillimanite (sill), kyanite (ky), ilmenite, rutile, and quartz (q) are taken to be pure phases. The solution model of White et al. [111] is used for garnet, biotite, chlorite, chloritoid, and staurolite. The solution model CHA1 [112, 113] is used for muscovite. The feldspar solution model is after Fuhrman and Lindsley [114]. In the computations, quartz is taken to be in excess and the fluid was assumed to be pure H_2O.

For interpreting the P-T pseudosection (Figures 10(g) and 10(h)), it was assumed that no part of the garnet dissolved during growth. The core to rim variations in measured compositions of garnet combined with the topology of X_{Fe}, X_{Ca}, and X_{Mn} isopleths suggests that the post-S_{S2} and pre-S_{S3} garnets grew in quartz-muscovite-biotite-garnet-sillimanite-ilmenite phase field due to prograde heating (640–690°C) at midcrustal pressures of 5.2–5.5 kbar (Figure 10(h)). The P-T path is drawn in the direction of increasing X_{Ca} (=Ca/(Ca+Fe+Mg) and X_{Fe} (=Fe/Fe+Mg), decreasing X_{Mn} (Mn/Mn+Ca+Fe +Mg), and higher volume% of garnet (Figure 10(h)). The reconstructed P-T path for the supracrustal rocks is similar to the one recorded by Maji et al. [60] but is strikingly different from the Early Mesoproterozoic granulite facies clockwise P-T path documented by Karmakar et al. [71], which is characterized by postpeak decompression and decompression-cooling for the Dumka anatectic basement gneisses.

7. Monazite Chemical Ages

High-quality U-Pb (zircon) data exist for the anatectic basement gneisses and granitoids (Domain I) in and around Dumka [66–70]. Monazite chemical dating by electron probe at the National Facility, Indian Institute of Technology, Kharagpur, was used to constrain the timing of the formation of the detachment zone and the steep-dipping shear zones. Th-U-Pb (total) ages in monazites were obtained following Montel et al. [115] from 9 samples selected from the three lithodemic units that make up Domains II–IV. Monazites in four mica schists of the supracrustal unit and three anatectic quartzofeldspathic gneisses including a garnet-sillimanite-K-feldspar metapelite (in the ensemble of high-grade basement rocks) and two blastoporphyritic granitoids were analyzed. X-ray element maps and back-scattered electron images were used to identify chemically distinct domains in representative monazites. A total of 213 spot ages in nine samples with error%[= 100 (2σ error in Ma/age in Ma)] < 6

were statistically resolved using Isoplot 3.0 [116]. The spot ages were calibrated against the standard Moacyr monazite dated to be 497 ± 10 Ma (EMP age, [117], p. 228); 487 ± Ma (TIMS age, [118]), and 509.3 ± 0.5 Ma (TIMS age [117], p. 228) (details in [119]). The details of analytical procedure are the same as in protocol I of Prabhakar [119]. The analytical data on monazites, spot ages, and 2σ errors are presented in Supplementary Material 1. Y and Th maps and textural contexts of age data are presented in Supplementary Materials 2, 3 respectively. Summary probability-density plots and selected X-ray element maps of monazites in the three lithodemic units are shown in Figure 11.

In Domains II to IV, Late Grenvillian chemical ages (1020–900 Ma) obtained in both mantles and outermost rims in zoned monazite grains, as well as in chemically homogenous monazites, are the most dominant age population in the samples (Figure 11). These monazites are typically parallel to and/or postdating (overgrowing?) metamorphic fabrics in the detachment zone (D3) foliations and steep-dipping shear zone foliation (D4 deformation) in granitoids and mica schists (Figure 11). These Grenvillian chemical ages also overlap with the U-Pb (zircon) lower intercept dates obtained in the basement gneisses from the core of the proposed MCC [61, 67, 68, 71]. Smaller populations of relict older ages (Figure 11), e.g., 1.6–1.4 Ga in the basement gneisses, 1.4–1.3 Ga in blastoporphyritic granitoids, and rare 1.3–1.2 Ga in mica schists are obtained in embayed rafts in the interiors of monazite grains. The Early Mesoproterozoic ages are interpreted to correspond with the early D1-D2 granulite facies metamorphism in the basement gneisses. The Mid Mesoproterozoic (1.4–1.3 Ga) cores possibly relate to the age of post-D2, pre-D3 emplacement of the granitoids intrusive into the basement gneisses. The 1.3–1.2 Ga ages in the mica schists are difficult to interpret; these could be detrital ages or instead mark an episode of midcrustal contact heating induced by granitoid emplacement.

The older ages are common in monazite grains lodged in dynamically recrystallized quartz-feldspar aggregates; monazites within mica aggregates record Grenvillian ages throughout all or most of the monazite grain. P-T pseudosection analyses in the mica schist and deformation microtextures indicate that these midcrustal shallowly dipping fabrics (Domain II) formed at T between 640 and 690°C (Figure 10(h)). The T values are lower (100–150°C) than the blocking temperature for intracrystalline U-Pb diffusion in monazite (>800°C; [120–122]). Clearly, therefore, in polychronous monazites, the Grenvillian age mantles and rims around older cores and entire grains formed due to the fluid-induced dissolution-precipitation process [123–125]. We suggest that monazites lodged in the "dry" quartz-feldspar aggregates better preserve older ages than those hosted in mica aggregates because of a lack of infiltrating fluids. In summary, the detachment zone and the steep shear zones were broadly coeval (within the 2σ errors of spot ages) with MCC formation in the Early Neoproterozoic age. The small subsidiary age peak at ~1060 Ma (Figure 11(c)) is difficult to interpret; however, Bhattacharya et al. [74] correlate this age with the early phase of crustal thickening during accretion of the CGC with the Singhbhum Craton.
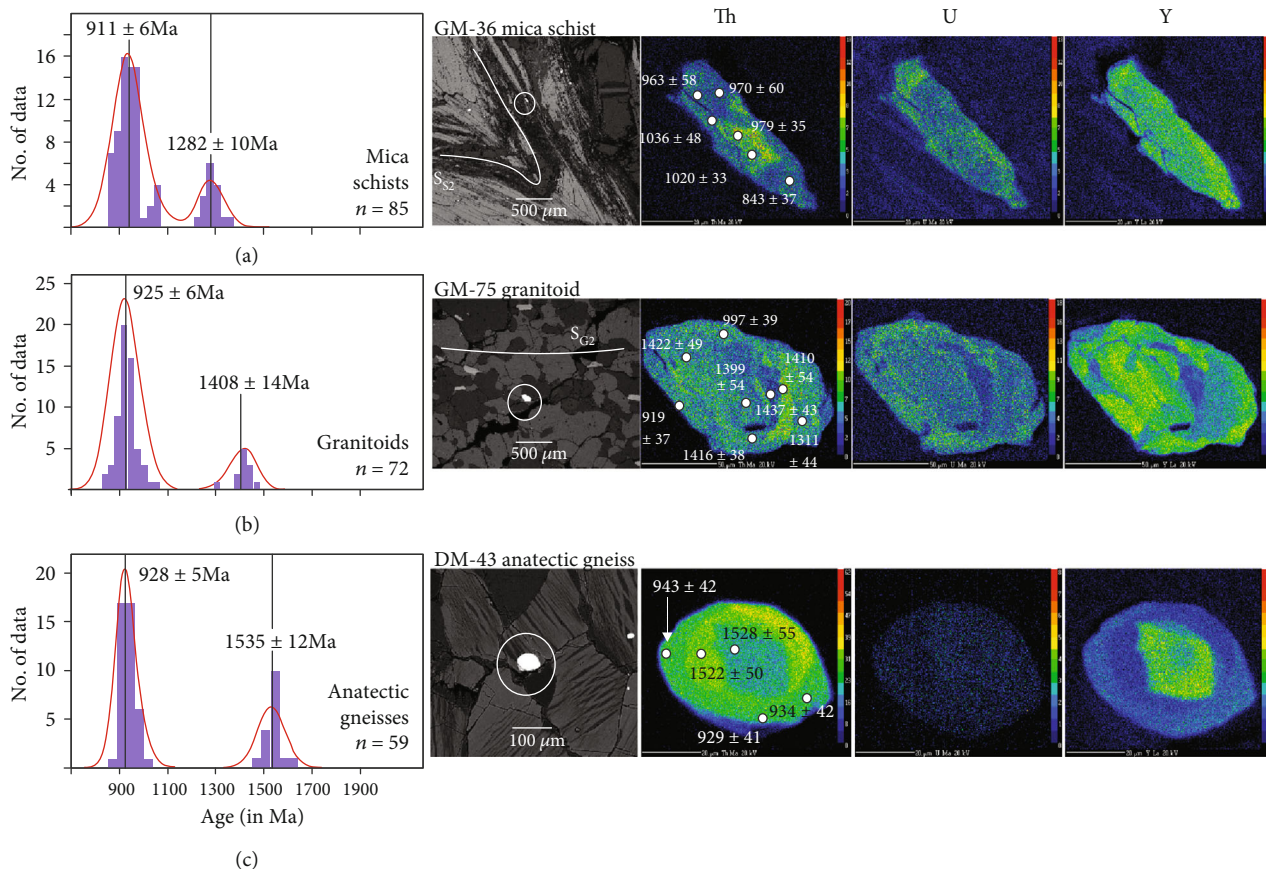
FIGURE 11: Probability-density maps of chemical age determinations in monazites (locations in Figure 1(b)). Alongside are representative monazite textures (back-scatter electron images) and X-ray element maps of Th, U, and Y in (a) mica schist; (b) granitoid; and (c) anatectic gneiss in the Giridih-Dumka-Deoghar-Chakai area. Spot ages (±2σ errors) in Ma are keyed to the Th maps. Additional monazite images in Supplementary Material 2.

8. Discussion

The Early Neoproterozoic accretion between the CGC with the Singhbhum Craton in the south occurred between 1.1 and 0.9 Ga [61, 73, 74]. The monazite chemical ages (this study) suggest that the D3 and D4 deformations that produced the CGC-MCC were contemporaneous with the convergent strain regime during the accretion. Documentation of domains of shallowly dipping foliations and recumbent/gently inclined folds truncated by steep-dipping ENE- to ESE-trending shear zones (Figures 1 and 2) has recently been made in large tracts of the CGC [62, 74]; these features are strikingly similar to the detachment zone of the proposed MCC in the Deoghar-Dumka-Chakai-Giridih area. Additionally, there are many areas in the CGC where the shallow-dipping fabrics are absent, exposing older basement rocks with steep, N-trending Mesoproterozoic fabrics. We propose that the CGC as a whole represents a coalescent agglomerate of regional-scale MCCs that developed within a convergent tectonic setting (Figure 12). After summarizing the major characteristics of each segment of the CGC-MCC, we propose a model for the formation of the CGC-MCC that integrates detachment zone formation (D3) and exhumation with transpressional shear zone development (D4).

8.1. The Core of the CGC-MCC. The granulite facies D1-D2 fabric-forming events in the basement gneisses (Domain I) involved pre-/syn-D1 voluminous melt generation manifested by metatexite layers in gneisses; the limited volumes of locally developed diatexites suggest that melt productivity waned considerably during the D2 deformation that produced the pervasive N-trending, steeply dipping S_{N2} gneissic layers in the anatectic gneisses. The Early Mesoproterozoic ages in the cores of monazites (1.5 – 1.4 Ga) in the anatectic gneisses (Figure 11(c)), consistent with U-Pb (zircon) upper intercept ages and Pb-Pb zircon ages (1.6-1.45 Ga), are inferred to be the age of emplacement of felsic orthogneisses [67–69] and granulite facies metamorphism in the gneisses in different parts of the CGC [61, 66, 71]. The 1.45 Ga cores in monazites in granitoids that share the D2 fabric with the gneisses are similar to the U-Pb (zircon) ages documented by Mukherjee et al. [68] in felsic orthogneisses from the Dumka area. Possibly, this age marks the culmination of Early Mesoproterozoic felsic emplacement and granulite facies metamorphism in the basement gneisses.

The CGC-MCC formation occurred in the Early Neoproterozoic, and therefore, the Early Mesoproterozoic gneisses and granitoids testify to earlier deformation, anatectic and metamorphic events unrelated to MCC formation; these
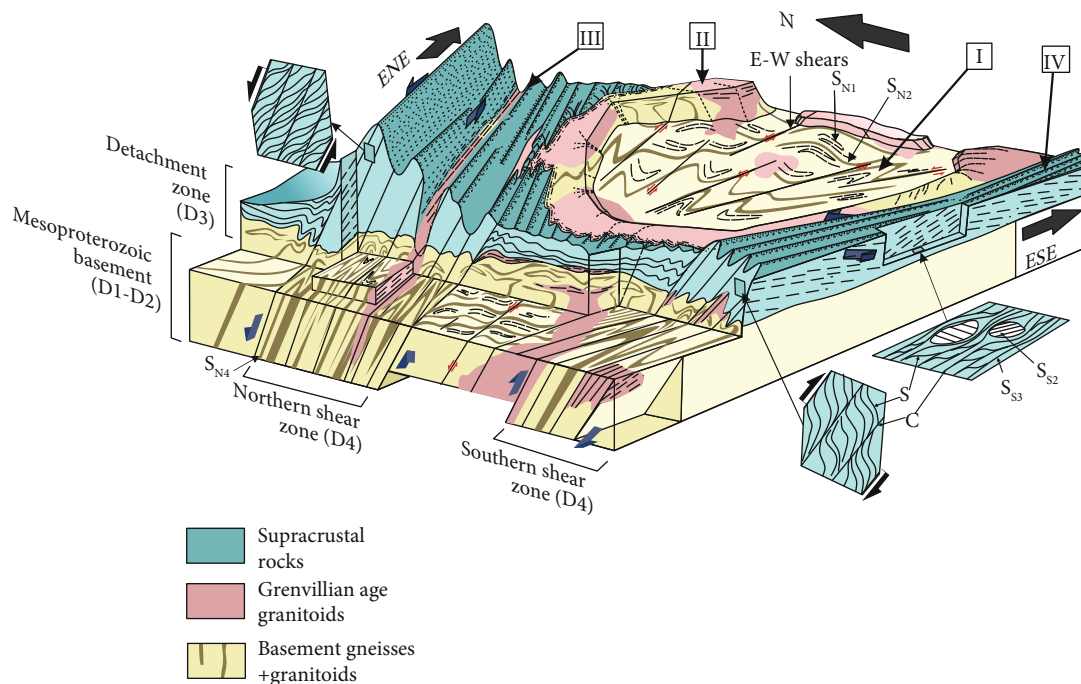
FIGURE 12: Schematic diagram showing the structural set up in the Giridih-Dumka-Deoghar-Chakai area.

rocks occur as enclaves within the Early Neoproterozoic granitoids exhumed beneath the shallowly dipping detachment zone (Figure 12). Mukherjee et al. [67] interpret the N-trending oldest D1-D2 composite fabric in the gneisses to correspond to the youngest deformation, despite the fact that two subsequent Early Neoproterozoic deformation events affected the CGC, as documented in this study, manifested by the shallowly dipping D3 fabric and the E-striking basement piercing D4 shear zones. For this reason, we consider the interpretation of Mukherjee et al. [67] to be simplistic.

8.2. The Hanging Wall of the CGC-MCC.
Extensive erosion in the CGC has removed much of the upper part of the hanging wall of the CGC-MCC. The surviving rocks comprise the amphibolite facies supracrustal unit that was deformed ductilely during the formation of the detachment zone, producing the penetrative shallowly dipping S_{S2} foliation in the rocks. The muscovite-biotite schist in the amphibolite facies supracrustal unit structurally overlying the basement gneisses is devoid of anatexis, and the rocks do not exhibit an intrusive relationship with the Mid Mesoproterozoic to Early Neoproterozoic granitoids [61, 62, 73] intrusive into the Early Mesoproterozoic basement gneisses. The shallow foliation in the supracrustal unit is a crenulation cleavage (S_{S2}) and is coplanar with the shallowly dipping D3 fabrics in the gneisses and granitoids (Figures 3(b)–3(d)). This suggests that the earlier history in the supracrustal unit was not shared with the granitoids that lack the earlier fabrics or the basement gneisses in which the earlier fabrics formed at granulite facies conditions. In the muscovite-biotite schists, the lack of 1.6–1.5 Ga monazite ages corresponding

to the D1-D2 anatectic conditions experienced by the Early Mesoproterozoic basement gneisses suggests that the Grenvillian age supracrustal rocks in the flat-lying/shallow-dipping carapace (Figure 11(a)) constitute an allochthonous unit transported over the basement gneisses and granitoids. Also, the dP/dT slope of the post-D3 prograde P-T path reconstructed for the supracrustal unit is gentler than those recorded in zones of accretion of cold crustal blocks. It is necessary therefore to invoke heat sources to explain the metamorphic evolution in the nonanatectic amphibolite facies supracrustal unit. We suggest that the tectonic emplacement of the supracrustal unit over the basement closely followed intrusion of the Grenvillian age granitoids. Release of heat from the cooling granitoids intrusive into the basement gneisses provided the necessary heat for the prograde heating.

8.3. The Detachment Zone.
The deformation microstructures in granitoid mylonites in the detachment zone juxtaposed against the supracrustal unit are noteworthy. Domain II granitoid mylonites comprise core-mantle-structured feldspar porphyroclasts in finer grained matrices consisting of aggregates of moderately inequant grains of polygonized quartz and feldspar and myrmekites. The grains in the matrix are internally strained (undulatory extinction, subgrains, deformation twins, and bent twin lamellae) and share mildly curved grain/phase boundaries, although triple junctions are common. The porphyroclasts exhibit undulatory extinction and rare subgrains in magmatic cores of feldspars. The microstructural relations, in combination with the crystallographic data, suggest deformation by dislocation creep with some recrystallization.

However, deformation temperature in excess of 650°C is precluded due to the absence of high-T deformation microstructures (such as chessboard twinning in quartz [126], randomly dispersed interphase boundaries [127], suprasolidus deformation microstructures (such as rationally developed faces of minerals growing into neighboring quartz and K-feldspar; [128]), imbrications of euhedral feldspar aggregates [129], and optically homogenous quartz grain piercing feldspars [130, 131]. We speculate therefore that emplacement of the supracrustal unit and formation of the detachment zone postdated intrusion of Early Neoproterozoic granitoids, but the cooling of the granitoids outlasted emplacement.

Results of P-T pseudosection analysis imply that the supracrustal unit experienced crustal thickening up to 16-18 km (5.2 – 5.5 kbar lithostatic pressure; Figure 10(h)) syn-to-post-D3 deformation/metamorphism in the detachment zone. Crustal thickening can result in collapse manifest as vertical thinning, horizontal extension, and the formation of mid-crustal flat-lying detachment zone even in convergent settings [6, 21, 132–135]. In the CGC, vorticity estimates for the shallow-dipping granitoids (Figures 9(a)–9(c)) point to considerable influence of a pure shear component during D3 fabric formation in the detachment zone (cf., [136]). Also, rare shear sense indicators in the carapace consistently show a core-up sense of movement (Figure 5(e)). We suggest therefore that the line of demarcation between the detachment zone that experienced D3 deformation and the underlying Domain I basement gneisses (Figure 2) unaffected by D3 is a decollement that formed due to extension [136–138]. Similar Grenvillian age structures are reported from the central parts of the CGC [62], indicating that most of the crustal block making up the CGC evolved together and was involved in the formation of a regional-scale MCC.

Results of our crystallographic analyses and vorticity estimations from rigid porphyroclasts indicate that deformation within the detachment zone was heterogeneous. The rare stretching lineations in the detachment zone do not show any decipherable map pattern, neither linear nor radial (Figures 2(b) and 3(e)), and the axes of D3 recumbent folds in the basement gneisses are similarly scattered (Figure 3(d)). This variable distribution of stretching lineations and recumbent fold axes is unusual in continental MCCs, in which stretching lineations normally display linear map patterns related to the flow direction of material during extension [1]. In the central CGC, the stretching lineations in the shallow-dipping detachment zone consistently plunge towards NW and SE [62], suggesting definite strain patterns associated with the detachment zone in these regions. The variable orientations of the shallow lineations in the Giridih-Dumka-Deoghar-Chakai quadrant are therefore difficult to explain and are possibly best justified by considering local variations in strain, although radial distribution of stretching lineation could be related to a diapiric rise of plutons [139]. Also, deeper down from the detachment, the bulk strain and relative contribution of simple shear is likely to decrease, and this could influence the dispersal of the stretching axis if different depths exposed by erosion are sampled.

The map pattern of the study area (Figures 1(b) and 2) with lithostructural 'islands' of Domain II rocks within Domain I and vice versa is similar to map patterns of regional-scale MCCs [140, 141] in which the detachment zone has been folded on a kilometer- scale by steeply inclined to upright open folds commonly termed 'corrugations' [142]. The fold axes of these corrugations are subparallel with the stretching direction in the detachment zones of the MCC [140, 142, 143]. However, although the shallowly dipping S_{S2} fabric in the supracrustal rocks and the S_{N3} fabric in the gneisses within the area display outcrop-scale upright folds, no large-scale corrugations were observed or could be inferred at the present level of exposure of the detachment zone in Domain II. We interpret the locally developed upright folds in the supracrustal rocks and basement gneisses as effects of the formation of the steeply dipping transpressional shear zones (D4).

8.4. The Steep Shear Zones. The orientations of folds in transtensional and transpressional shear zones have been investigated using numerical strain modeling [144–148]. In vertical/steep-dipping transtensional shear zones, folds on flat/shallow-dipping planes initiate at angles >45° with the shear zone wall, and the hinge rotation determined by the instantaneous stretching axes and the divergence vector are small for pure shear-dominated systems even at infinitely high strain and moderate for wrench-dominated system [146]. By contrast, in vertical/steep-dipping transpressional shear zones, fold hinges rotate increasingly towards the shear zone wall [100, 149–151] with higher bulk strain, although significant simple shear strain is necessary to rotate fold hinges parallel to the maximum finite stretch ([147], and references therein). In the ENE-/NE-trending and ESE-trending shear zones in Domains III and IV of the Giridih-Dumka-Deoghar-Chakai area (Figure 2(a)), the subhorizontal/gently plunging and noncylindrical hinge lines of E-/ESE-trending D4 upright folds on flat-lying/shallow-dipping schistosity in the supracrustal unit (Figures 3(h) and 3(j)) share low-angle obliquity with the stretching lineations of the granitoid mylonites (Figures 3(e) and 3(i)) and the walls of the two hosting shear zones. The shear zones therefore are transpressive in nature. The small variation in the plunges of the stretching lineations in the Domain III and IV granitoids (Figures 3(e) and 3(i)) indicates regional-scale heterogeneity in deformation strain within the shear zones (cf. [152]). Both shear zones exhibit sinistral kinematics. In the northern shear zone, the VNS is subhorizontal, implying that the shear zone follows a monoclinic symmetry that is consistent with the results of our crystallographic vorticity analyses; however, stretching lineation orientations (Figure 3(i)) and crystallographic data (Figure 8(e)) indicate that the deformation in the southern shear zone was at least locally triclinic. Although both shear zones dip steeply to the north, opposite sense of shear is exhibited in the section of the two shear zones; N-down for the northern shear zone and S-down for the southern shear zone (Figure 12). Since Grenvillian monazite ages in mica schists hosted within both shear zones overlap, we suggest the two shear zones were contemporaneous. The shear zones possibly constitute a sinistral freeway [153], although deep weathering and soil

cover near the projected junction (NW of Giridih) prevent field confirmation.

Subhorizontal stretching lineations in transpressive shear zones with significant finite strain indicate a high simple shear component of deformation [77, 144, 154]. Vorticity analysis of the northern shear zone granitoids on the other hand produced Wm values intermediate to pure shear and simple shear (Figures 9(d)–9(f)). Li and Jiang [106] have demonstrated that the vorticity estimates from rigid porphyroclasts could be simple shear dominated even when the Wm values range between 0.50 and 0.85. The EBSD results (Figures 8(c)–8(f)) support the vorticity estimations and suggest a significant pure shear component for the D4 deformation in both Domains III and IV.

Therefore, if the Wm values are considered to be relatively indicative of the vorticity for the northern shear zone, the average of the range estimated is Wm = 0.67. This value is tentatively used in the kinematic modeling of the shear zone following the triclinic transpression with oblique extrusion model of Fernandez and Diaz-Azpiroz [155] using the software GTOE (version 2) (Carlos Fernandez, personal communication). The following parameters are used in modeling: φ is the angle between the simple shear direction and the strike of the shear zone, υ is the angle between dip of the shear zone and the extrusion direction due to the coaxial component, W_k is Truesdell's [99] kinematic vorticity number, and K is the log shape parameter of a coaxial component. The model yields the principal quadratic extensions ($\lambda_1 \geq \lambda_2 \geq \lambda_3$) and their orientations with respect to the external reference frame fixed to the shear zone under investigation. The stretching lineation is approximated to the X axis (λ_1) of the finite strain ellipsoid and the foliation is approximated to the XY plane (perpendicular to the Z axis, λ_3).

Considering a vertical dip, a strike of 70°N and an average value $W_k = 0.67$ for the northern shear zone, a value of $\upsilon = 80$° (taking into account the gently plunging stretching lineations) was chosen. Three values of φ, $\varphi = 0$, 10, and 20 were modeled for, to account for the any uncertainty in the VNS estimation and three values of K were chosen, $K = 1$, 2, and 10^5 with 10^5 assumed to be tending to infinity. The results of the modeling are shown in Figures 9(g)–9(j). Figure 9(g) shows the log-Flinn diagram while Figures 9(h)–9(j) display the orientations of the X axis (λ_1) and XY planes (λ_3) of the resultant strain ellipsoids. The orientations of the X axis and the XY planes of all considered models show a fairly good fit to the natural data (Figure 3(e)), indicating that the shear zone may not be distinctly monoclinic but could incorporate some amount of triclinicity as well. The log-Flinn diagram (Figure 9(g)) shows that only small values of K ($K \approx 1$) are compatible with the natural data because as K values are increased, the plots move into the constrictional field of the diagram. This would lead to the formation of L-tectonites, which were not observed in the field.

Thus, both the northern and the southern shear zones are transpressional shear zones with a significant contribution of pure shear, in contrast to the strike-slip shear zones reported in other MCCs [10, 38, 40, 42, 45, 54]. Although structurally the shear zones (D4) developed subsequent to the detachment zone (D3) of the MCC, the contemporaneity in the

monazite age data in the two segments suggests that the shear zones played an integral part in the formation of the MCC in the Early Neoproterozoic.

8.5. The Model. The Early Neoproterozoic (1.1–0.9 Ga) D3-D4 deformations in the CGC are contemporaneous with the convergent strain regime during the accretion of the CGC with the composite of the Singhbhum Craton and the North Singhbhum Mobile belt [61, 73, 74]. The large-scale emplacement of granitoids in the CGC during the Grenvillian age is well documented [61, 62, 73]. Field relations and microstructural evidence suggest the deformation in these Grenvillian age granitoids (intrusive within the Early Mesoproterozoic basement gneisses and the older granitoids) outlasted their intrusion, but emplacement of the supracrustal rocks over the basement occurred with the cooling granitoids still being hot (Figure 10(h)). In other words, the intrusion of the granitoids preceded the formation of the MCC but the time interval between intrusion, thrusting, and detachment formation was likely to have been small (cf. [156]). Voluminous granitoid intrusion accelerates thermal weakening of the crust and renders it buoyant [157], promoting orogenic collapse and strain localization along shallow-dipping normal faults [1, 158]. Large-scale magmatic emplacements are thus likely associated with exhumation of the ductile crust [13, 159], and the Grenvillian-age granitoid intrusion within the CGC was possibly the trigger for the formation of the MCC.

Traditional models for the formation of the shallow dipping carapace within MCCs such as the "rolling-hinge detachments" [2, 9, 160] or "channel detachment" [8] models are based upon the relationships between the hanging wall and detachment. Within these models, the detachment fault results from the shallowing of originally steep-dipping normal faults which originate within the brittle upper crust. This mechanism is doubtful for MCCs with spatially expansive detachments such as the CGC, since the displacement along the envisaged normal faults would need to run hundreds of kilometers with exceedingly high rates of motion [6].

In the CGC, the detachment zone was formed in the ductile middle crust under high geothermal gradients and involved the allochthonous supracrustal unit and the screen of basement rocks immediately underlying it. We propose that the vertical shortening resulting from the collapse of a thickened crust combined with the buoyant rise of the basement dominated by granitoids was accommodated by strain localization and horizontal extension at the contact between the supracrustal unit and the basement, producing the shallow-dipping foliations in the granitoids (S_{G1}) and supracrustal rocks (S_{S2}) and recumbent folds within the anatectic gneisses (S_{N3}). Such localized extension during an overall convergent regime has been observed in other MCCs around the world ([1, 14, 161] and references therein). The shallow foliations produced within this zone would thus show variations such as in the amount of displacement, orientation of stretching lineations (Figure 3(c)) and recumbent fold axis (Figure 3(b)), and in shear sense indicators in different parts of the detachment, as observed within the CGC and in other MCCs as well [6, 162].

The crucial factor governing the mechanics of the CGC-MCC nevertheless is the presence of the regional-scale, subvertical sinistral transpressional Grenvillian age interconnected ENE- and ESE-trending shear zones (Domains III and IV, this study; HFSZ, [62]). The shear zones cut across all three lithodemic units of the CGC and reorient all earlier fabrics (Figure 12). Most numerical models for subvertical transpressional shear zones consider the shortening component of stress to be normal to the shear zone which is accommodated by vertical [150], lateral [144, 163], or oblique [155, 164–166] extrusion parallel to shear zone walls. Within the investigated N-down, sinistral, subvertical northern shear zone, gently plunging stretching lineations nearly parallel to the VNS imply a shear zone symmetry close to monoclinic symmetry. The coeval ENE-trending shear zone in the south shows identical sinistral kinematics and moderately plunging stretching lineations except for a S-down (reverse) sense of movement on the steeply N-dipping shear plane (Figures 3(i) and 7(f)). Although the subhorizontal stretching lineations suggest a lateral component of extrusion, the opposite movements in the profile sections are reminiscent of escape tectonics [167–170], wherein the entire block between the two shear zones is considered competent enough to be displaced vertically en masse, especially in a convergent regime.

We suggest the basement-piercing transpressional shear zones accommodated the bulk of the compression strain in the ductile middle and lower crust during the accretion of the CGC with the Singhbhum Craton in the Grenvillian age and developed contemporaneously or closely following the formation of the detachment. Vertical extrusion of the MCC segments between the shear zones was possibly at least partially compensated by the vertical shortening associated with orogenic collapse of the thickened crust. This would account for the absence of considerable changes in the metamorphic grade of the basement rocks or the supracrustal rocks due to exhumation. There was also a considerable component of lateral stretch associated with the subvertical shear zones as modeled in Figures 9(g) and 9(h). MCCs with greater horizontal movement within the core as compared to vertical motion have been previously modeled [2, 171] but without considering the contribution of shear zones.

Thus, the CGC provides a new example of a metamorphic core complex that was developed during synconvergent extension (Figure 12). This type of deformation is well documented within the modern Himalaya (e.g., [172]) but is increasingly recognized in the geologic record, whether in core complexes previously traditionally thought to form entirely postconvergence (e.g., Naxos; [41]) or in midcrustal domes interpreted to form only during collision (e.g., the southern Appalachians; [173]). With this context, recognition of synconvergent extension in the CGC suggests that it may be worthwhile to reconsider the structural evolution of high-grade Precambrian complexes around the world.

Data Availability

All the data used in this study are incorporated within the article and in the supplementary material provided along with the article. No other data from any other source was used in the research described in the article.

Disclosure

The article forms a part of the doctoral dissertation of NS. SM and SS carried out parts of the work during their tenure at IIT Kharagpur as part of their Masters programs.

Conflicts of Interest

The authors declare that they have no conflicts of interest.

Acknowledgments

Supplementary Materials

Supplementary 1. Supplementary Data[1]: monazite composition and chemical ages (±2σ) in Ma in the nine analyzed samples.

Supplementary 2. Supplementary Data[2]: representative monazite textures (back-scatter electron images) and X-ray element maps of Th, U, and Y in mica schist, granitoid, and anatectic gneiss in the Giridih-Dumka-Deoghar-Chakai area. Spot ages (±2σ) in Ma are keyed to the Th maps.

Supplementary 3. Supplementary Data[3]: textural context and chemical ages in monazite dated samples (locations in Figure 1)

References

[1] D. L. Whitney, C. Teyssier, P. F. Rey, and W. R. Buck, "Continental and oceanic core complexes," *Geological Society of America Bulletin*, vol. 125, no. 3-4, pp. 273–298, 2013.

[2] J.-P. Brun and J. van den Driessche, "Extensional gneiss domes and detachment fault systems–structure and kinematics," *Bulletin de la Société for Géologique de France*, vol. 165, no. 6, pp. 519–530, 1994.

[3] F. J. Cooper, J. P. Platt, R. Anczkiewicz, and M. J. Whitehouse, "Footwall dip of a core complex detachment fault: thermobarometric constraints from the northern Snake range (basin and range, USA)," *Journal of Metamorphic Geology*, vol. 28, no. 9, pp. 997–1020, 2010.

[4] G. A. Davis and G. S. Lister, "Detachment faulting in continental extension; perspectives from the southwestern U.S. Cordillera," *Geological Society of America Special Papers*, vol. 218, pp. 133–160, 1988.

[5] E. L. Miller, P. B. Gans, and J. Garlin, "The Snake Range décollement: an exhumed Mid-Tertiary ductile-brittle transition," *Tectonics*, vol. 2, no. 3, pp. 239–263, 1983.

[6] J. P. Platt, W. M. Behr, and F. J. Cooper, "Metamorphic core complexes: windows into the mechanics and rheology of the crust," *Journal of the Geological Society of London*, vol. 172, no. 1, pp. 9–27, 2015.

[7] P. F. Rey, C. Teyssier, S. C. Kruckenberg, and D. L. Whitney, "Viscous collision in channel explains double domes in metamorphic core complexes," *Geology*, vol. 39, no. 4, pp. 387–390, 2011.

[8] C. Teyssier, E. Ferré, D. L. Whitney, B. Norlander, O. Vanderhaeghe, and D. Parkinson, "Flow of partially molten crust and origin of detachments during collapse of the cordilleran orogen," *Geological Society, London, Special Publications*, vol. 245, no. 1, pp. 39–64, 2005.

[9] B. Wernicke and G. J. Axen, "On the role of isostasy in the evolution of normal fault systems," *Geology*, vol. 16, no. 9, pp. 848–851, 1988.

[10] D. Gasser, E. Bruand, K. Stüwe et al., "Formation of a metamorphic complex along an obliquely convergent margin: structural and thermochronological evolution of the Chugach metamorphic complex, southern Alaska," *Tectonics*, vol. 30, no. 2, 2011.

[11] H. Fritz, E. Wallbrecher, A. A. Khudeir, F. Abu el Ela, and D. R. Dallmeyer, "Formation of Neoproterozoic metamorphic complex during oblique convergence (Eastern Desert, Egypt)," *Journal of African Earth Sciences*, vol. 23, no. 3, pp. 311–329, 1996.

[12] B. Zhang, Z. Chai, C. Y. Yin et al., "Intra-continental transpression and gneiss doming in an obliquely convergent regime in SE Asia," *Journal of Structural Geology*, vol. 97, pp. 48–70, 2017.

[13] M. Aoya, S. R. Wallis, K. Terada et al., "North-south extension in the Tibetan crust triggered by granite emplacement," *Geology*, vol. 33, no. 11, pp. 853–856, 2005.

[14] P. Rey, O. Vanderhaeghe, and C. Teyssier, "Gravitational collapse of the continental crust: definition, regimes and modes," *Tectonophysics*, vol. 342, no. 3-4, pp. 435–449, 2001.

[15] M. P. Searle and T. N. Lamont, "Compressional metamorphic core complexes, low-angle normal faults and extensional fabrics in compressional tectonic settings," *Geological Magazine*, vol. 157, pp. 101–118, 2020.

[16] W. R. Buck and D. Sokoutis, "Analogue model of gravitational collapse and surface extension during continental convergence," *Nature*, vol. 369, no. 6483, pp. 737–740, 1994.

[17] B. C. Burchfiel and L. H. Royden, "North–south extension within the convergent Himalayan region," *Geology*, vol. 13, no. 10, pp. 679–682, 1985.

[18] P. J. Coney and T. A. Harms, "Cordilleran metamorphic core complexes: Cenozoic extensional relics of Mesozoic compression," *Geology*, vol. 12, no. 9, pp. 550–554, 1984.

[19] J. F. Dewey, "Extensional collapse of orogens," *Tectonics*, vol. 7, no. 6, pp. 1123–1139, 1988.

[20] P. England and G. Houseman, "Extension during continental convergence, with application to the Tibetan Plateau," *Journal of Geophysical Research*, vol. 94, no. B12, p. 17561, 1989.

[21] T. Rivers, "Upper-crustal orogenic lid and mid-crustal core complexes: signature of a collapsed orogenic plateau in the hinterland of the Grenville Province1This article is one of a series of papers published inCJES Special Issue: In honour

of Ward Nealeon the theme of Appalachian and Grenvillian geology," *Canadian Journal of Earth Sciences*, vol. 49, no. 1, pp. 1–42, 2012.

[22] T. Rivers and W. M. Schwerdtner, "Post-peak evolution of the Muskoka domain, Western Grenville Province: ductile detachment zone in a crustal-scale metamorphic core complex," *Geoscience Canada*, vol. 42, no. 4, pp. 403–436, 2015.

[23] M. S. Wong, M. L. Williams, J. M. McLelland, M. J. Jercinovik, and J. Kowalkoski, "Late Ottawan extension in the eastern Adirondack highlands: evidence from structural studies and zircon and monazite geochronology," *Geological Society of America Bulletin*, vol. 124, no. 5-6, pp. 857–869, 2012.

[24] J. P. Burg, M. Brunel, D. Gapais, G. M. Chen, and G. H. Liu, "Deformation of leucogranites of the crystalline Main Central Sheet in southern Tibet (China)," *Journal of Structural Geology*, vol. 6, no. 5, pp. 535–542, 1984.

[25] J. M. Crespi, Y.-C. Chan, and M. S. Swaim, "Synorogenic extension and exhumation of the Taiwan hinterland," *Geology*, vol. 24, no. 3, pp. 247–250, 1996.

[26] E. H. Hartz, A. Andresen, K. V. Hodges, and M. W. Martin, "Syncontractional extension and exhumation of deep crustal rocks in the East Greenland Caledonides," *Tectonics*, vol. 20, no. 1, pp. 58–77, 2001.

[27] K. V. Hodges, R. R. Parrish, T. B. Housh et al., "Simultaneous Miocene extension and shortening in the Himalayan orogen," *Science*, vol. 258, no. 5087, pp. 1466–1470, 1992.

[28] J. Malavielle, "Late orogenic extension in mountain belts: insights from the basin and range and the late Paleozoic Variscan belt," *Tectonics*, vol. 12, no. 5, pp. 1115–1130, 1993.

[29] J. P. Platt, "Dynamics of orogenic wedges and the uplift of high-pressure metamorphic rocks," *Geological Society of America Bulletin*, vol. 79, pp. 1037–1105, 1986.

[30] L. Ratschbacher, W. Frisch, F. Neubauer, S. M. Schmid, and J. Neugebauer, "Extension in compressional orogenic belts: the eastern Alps," *Geology*, vol. 17, no. 5, pp. 404–407, 1989.

[31] S. P. Long, S. N. Thomson, P. W. Reiners, and R. V. Di Fiori, "Synorogenic extension localized by upper-crustal thickening: an example from the late cretaceous Nevadaplano," *Geology*, vol. 43, no. 4, pp. 351–354, 2015.

[32] G. Axen, J. Selverstone, T. Byrne, and J. M. Fletcher, "If the strong lower crust leads, will the weak crust follow?," *GSA Today*, vol. 8, no. 12, pp. 1–8, 1998.

[33] L. Le Pourhiet, B. Huet, D. A. May, L. Labrousse, and L. Jolivet, "Kinematic interpretation of the 3D shapes of metamorphic core complexes," *Geochemistry, Geophysics, Geosystems*, vol. 13, no. 9, article Q09002, 2012.

[34] N. S. Mancktelow and T. L. Pavlis, "Fold-fault relationships in low-angle detachment systems," *Tectonics*, vol. 13, no. 3, pp. 668–685, 1994.

[35] P. Molnar, "Gravitational instability of mantle lithosphere and core complexes," *Tectonics*, vol. 34, no. 3, pp. 478–487, 2015.

[36] P. F. Rey, L. Mondy, G. Duclaux et al., "The origin of contractional structures in extensional gneiss domes," *Geology*, vol. 45, no. 3, pp. 263–266, 2017.

[37] S. Wdowinski and G. J. Axen, "Isostatic rebound due to tectonic denudation: a viscous flow model of a layered lithosphere," *Tectonics*, vol. 11, no. 2, pp. 303–315, 1992.

[38] A. G. Baines, M. J. Cheadle, H. J. B. Dick et al., "Mechanism for generating the anomalous uplift of oceanic core

complexes: Atlantis Bank, southwest Indian ridge," *Geology*, vol. 31, no. 12, pp. 1105–1108, 2003.

[39] J. R. Cann, D. K. Blackman, D. K. Smith et al., "Corrugated slip surfaces formed at ridge-transform intersections on the Mid- Atlantic Ridge," *Nature*, vol. 385, no. 6614, pp. 329–332, 1997.

[40] D. A. Foster, P. T. Doughty, T. J. Kalakay et al., "Kinematics and timing of exhumation of metamorphic core complexes along the Lewis and Clark fault zone, northern Rocky Mountains, USA," in *Exhumation Associated with Continental Strike-Slip Fault Systems. Geological Society of America Special Paper*, S. M. Roeske, A. B. Till, D. A. Foster, and J. C. Sample, Eds., vol. 434, pp. 207–231, 2007.

[41] T. N. Lamont, M. P. Searle, D. J. Waters et al., "Compressional origin of the Naxos metamorphic core complex, Greece: structure, petrology, and thermobarometry," *Geological Society of America Bulletin*, 2019.

[42] R. R. McFadden, C. Teyssier, C. S. Siddoway, D. L. Whitney, and C. M. Fanning, "Oblique dilation, melt transfer, and gneiss dome emplacement," *Geology*, vol. 38, no. 4, pp. 375–378, 2010.

[43] C. R. Ranero and T. J. Reston, "Detachment faulting at ocean core complexes," *Geology*, vol. 27, no. 11, pp. 983–986, 1999.

[44] B. E. Tucholke, J. Lin, and M. Kleinrock, "Megamullions and mullion structure defining oceanic metamorphic core complexes on the mid-Atlantic ridge," *Journal of Geophysical Research*, vol. 103, no. B5, pp. 9857–9866, 1998.

[45] D. L. Whitney, C. Teyssier, and M. T. Heizler, "Gneiss domes, metamorphic core complexes, and wrench zones: thermal and structural evolution of the Niğde massif, Central Anatolia.," *Tectonics*, vol. 26, article TC5002, 2007.

[46] A. I. Chemenda, M. Mattauer, J. Malavieille, and A. N. Bokun, "A mechanism for syn-collisional rock exhumation and associated normal faulting: results from physical modelling," *Earth and planetary science letters*, vol. 132, no. 1-4, pp. 225–232, 1995.

[47] S. E. Meyer, C. Passchier, T. Abu-Alam, and K. Stüwe, "A strike-slip core complex from the Najd fault system, Arabian shield," *Terra Nova*, vol. 26, no. 5, pp. 387–394, 2014.

[48] F. Neubauer, R. D. Dallmeyer, I. Dunkl, and D. Schirnik, "Late cretaceous exhumation of the metamorphic Gleinalm dome, eastern Alps: kinematics, cooling history and sedimentary response in a sinistral wrench corridor," *Tectonophysics*, vol. 242, no. 1-2, pp. 79–98, 1995.

[49] M. R. Scharman, T. L. Pavlis, E. M. Day, and L. J. O'Driscoll, "Deformation and structure in the Chugach metamorphic complex, southern Alaska: crustal architecture of a transpressional system from a down plunge section," *Geosphere*, vol. 7, no. 4, pp. 992–1012, 2011.

[50] F. Storti, R. E. Holdsworth, and F. Salvini, "Intraplate strike-slip deformation belts," *Geological Society of London Special Publication*, vol. 210, pp. 1–14, 2003.

[51] A. B. Till, S. Roeske, J. C. Sample, and D. Foster, "Exhumation associated with continental strike-slip fault systems," *Geological Society of America Special Paper*, vol. 434, pp. 233–264, 2007.

[52] X. Wang and F. Neubauer, "Orogen-parallel strike-slip faults bordering metamorphic core complexes: the Salzach–Enns fault zone in the Eastern Alps, Austria," *Australian Journal of Structural Geology*, vol. 20, no. 6, pp. 799–818, 1998.

[53] Z. Xu, Q. Wang, A. Pêcher et al., "Orogen–parallel ductile extension and extrusion of the greater Himalaya in the late Oligocene and Miocene," *Tectonics*, vol. 32, no. 2, pp. 191–215, 2013.

[54] Z. Q. Xu, Q. Wang, Z. H. Cai et al., "Kinematics of the Tengchong terrane in SE Tibet from the late Eocene to early Miocene: insights from coeval mid-crustal detachments and strike-slip shear zones," *Tectonophysics*, vol. 665, pp. 127–148, 2015.

[55] S. Cao and F. Neubauer, "Deep crustal expressions of exhumed strike-slip fault systems: shear zone initiation on rheological boundaries," *Earth Science Reviews*, vol. 162, pp. 155–176, 2016.

[56] T. M. Mahadevan, *Geology of Bihar and Jharkhand*, Geological Society of India, Bangalore, 2002.

[57] M. Ramakrishnan and R. Vaidyanadhan, "Geology of India, Volume 1," Geological Society of India, Bangalore, India, 2008.

[58] N. Chatterjee and N. C. Ghose, "Extensive early Neoproterozoic high-grade metamorphism in north Chotanagpur gneissic complex of the central Indian tectonic zone," *Gondwana Research*, vol. 20, no. 2-3, pp. 362–379, 2011.

[59] N. Chatterjee, M. Banerjee, A. Bhattacharya, and A. K. Maji, "Monazite chronology, metamorphism–anatexis and tectonic relevance of the mid- Neoproterozoic Eastern Indian Tectonic Zone," *Precambrian Research*, vol. 179, no. 1-4, pp. 99–120, 2010.

[60] A. K. Maji, S. Goon, A. Bhattacharya, B. Mishra, S. Mahato, and H. J. Bernhardt, "Proterozoic polyphase metamorphism in the Chhotanagpur Gneissic Complex (India), and implication for trans-continental Gondwanaland correlation," *Precambrian Research*, vol. 162, pp. 385–402, 2008.

[61] S. Rekha, D. Upadhyay, A. Bhattacharya et al., "Lithostructural and chronological constraints for tectonic restoration of Proterozoic accretion in the eastern Indian Precambrian shield," *Precambrian Research*, vol. 187, no. 3-4, pp. 313–333, 2011.

[62] N. Sequeira and A. Bhattacharya, "Early Neoproterozoic deformation kinematics in the Chottanagpur gneiss complex (eastern India): evidence from the curvilinear Hundru falls shear zone," *Lithosphere*, 2020.

[63] H. N. Bhattacharya, A. Chakraborty, and B. Bhattacharya, "Significance of transition between Talchir formation and Karharbari formation in lower Gondwana basin evolution – a study in West Bokaro coal basin, Jharkhand, India," *Journal of Earth System Science*, vol. 114, no. 3, pp. 275–286, 2005.

[64] R. W. Kent, S. P. Kelley, and M. S. Pringle, "Mineralogy and $^{40}Ar/^{39}Ar$ geochronology of orangeites (group II kimberlites) from the Damodar valley, eastern India," *Mineralogical Magazine*, vol. 62, no. 3, pp. 313–323, 1998.

[65] R. W. Kent, M. S. Pringle, R. D. Muller, A. D. Saunders, and N. C. Ghose, "$^{40}Ar/^{39}Ar$ geochronology of the Rajmahal basalts, India, and their relationship to the Kerguelen plateau," *Journal of Petrology*, vol. 43, no. 7, pp. 1141–1153, 2002.

[66] S. K. Acharyya, "The nature of Mesoproterozoic central Indian tectonic zone with exhumed and reworked older granulites," *Gondwana Research*, vol. 6, no. 2, pp. 197–214, 2003.

[67] S. Mukherjee, A. Dey, S. Sanyal, M. Ibanez-Mejia, U. Dutta, and P. Sengupta, "Petrology and U–Pb geochronology of zircon in a suite of charnockitic gneisses from parts of the

Chotanagpur Granite Gneiss Complex (CGGC): evidence for the reworking of a Mesoproterozoic basement during the formation of the Rodinia supercontinent," *Geological Society of London Special Publication*, vol. 457, pp. 197–232, 2017.

[68] S. Mukherjee, A. Dey, M. Ibanez-Mejia, S. Sanyal, and P. Sengupta, "Geochemistry, U-Pb geochronology and Lu-Hf isotope systematics of a suite of ferroan (A-type) granitoids from the CGGC: evidence for Mesoproterozoic crustal extension in the east Indian shield," *Precambrian Research*, vol. 305, pp. 40–63, 2018.

[69] S. Mukherjee, A. Dey, S. Sanyal, M. Ibanez-Mejia, and P. Sengupta, "Bulk rock and zircon geochemistry of granitoids from the Chotanagpur granite gneissic complex (CGGC): implications for the late Paleoproterozoic continental arc magmatism in the east Indian shield," *Contribution to Mineralogy and Petrology*, vol. 174, no. 8, 2019.

[70] S. Sanyal and P. Sengupta, "Metamorphic evolution of the Chotanagpur granite gneiss complex of the east Indian shield: current status," *Geological Society, London, Special Publications*, vol. 365, no. 1, pp. 117–145, 2012.

[71] S. Karmakar, S. Bose, A. B. Sarbadhikari, and K. Das, "Evolution of granulite enclaves and associated gneisses from Purulia, Chhotanagpur Granite Gneiss Complex, India: Evidence for 990–940 Ma tectonothermal event(s) at the eastern India cratonic fringe zone," *Journal of Asian Earth Sciences*, vol. 41, no. 1, pp. 69–88, 2011.

[72] N. Chatterjee, J. L. Crowley, and N. C. Ghose, "Geochronology of the 1.55 Ga Bengal anorthosite and Grenvillian metamorphism in the Chotanagpur Gneissic Complex, eastern India," *Precambrian Research*, vol. 161, no. 3-4, pp. 303–316, 2008.

[73] A. Bhattacharya, H. H. Das, E. Bell et al., "Restoration of late Neoarchean–early Cambrian tectonics in the Rengali orogen and its environs (eastern India): the Antarctic connection," *Lithos*, vol. 263, pp. 190–212, 2016.

[74] A. Bhattacharya, S. Rekha, N. Sequeira, and A. Chatterjee, "Transition from shallow to steep foliation in the early Neoproterozoic Gangpur accretionary orogen (eastern India): mechanics, significance of mid-crustal deformation, and case for subduction polarity reversal?," *Lithos*, vol. 348-349, p. 105196, 2019.

[75] B. Goswami and C. Bhattacharyya, "Petrogenesis of shoshonitic granitoids, eastern India: implications for the late Grenvillian post-collisional magmatism," *Geoscience Frontiers*, vol. 5, no. 6, pp. 821–843, 2014.

[76] R. Hielscher and H. Schaeben, "A novel pole figure inversion method: specification of theMTEXalgorithm," *Journal of Applied Crystallography*, vol. 41, no. 6, pp. 1024–1037, 2008.

[77] B. Tikoff and D. Greene, "Stretching lineations in transpressional shear zones: an example from the Sierra Nevada batholith, California," *Journal of Structural Geology*, vol. 19, no. 1, pp. 29–39, 1997.

[78] Z. D. Michels, S. C. Kruckenberg, J. R. Davis, and B. Tikoff, "Determining vorticity axes from grain-scale dispersion of crystallographic orientations," *Geology*, vol. 43, no. 9, pp. 803–806, 2015.

[79] M. Díaz-Azpiroz, C. Fernández, and D. M. Czeck, "Are we studying deformed rocks in the right sections? Best practices in the kinematic analysis of 3D deformation zones," *Journal of Structural Geology*, vol. 125, pp. 218–225, 2019.

[80] D. Jiang and P. F. Williams, "High-strain zones: a unified model," *Journal of Structural Geology*, vol. 20, no. 8, pp. 1105–1120, 1998.

[81] T. Mac Cready, "Misalignment of quartz c-axis fabrics and lineations due to oblique final strain increments in the Ruby Mountains core complex, Nevada," *Journal of Structural Geology*, vol. 18, no. 6, pp. 765–776, 1996.

[82] W. Sullivan, R. Beane, E. Beck, W. Fereday, and A. Roberts-Pierel, "Testing the transpression hypothesis in the western part of the Cheyenne belt, medicine Bow Mountains, southeastern Wyoming," *Rocky Mountain Geology*, vol. 46, no. 2, pp. 111–135, 2011.

[83] P. Xypolias, N. Gerogiannis, V. Chatzaras et al., "Using incremental elongation and shearing to unravel the kinematics of a complex transpressional zone," *Journal of Structural Geology*, vol. 115, pp. 64–81, 2018.

[84] S. M. Schmid and M. Casey, "Complete fabric analysis of some commonly observed quartz c-axis patterns," in *Mineral and Rock Deformation: Laboratory Studies (The Paterson Volume)*, B. E. Hobbs and H. C. Heard, Eds., pp. 263–268, 1986.

[85] A. Minor, E. Rybacki, M. Sintubin, S. Vogel, and H.-R. Wenk, "Tracking mechanical Dauphiné twin evolution with applied stress in axial compression experiments on a low-grade metamorphic quartzite," *Journal of Structural Geology*, vol. 112, pp. 81–94, 2018.

[86] G. E. Lloyd, "Microstructural evolution in a mylonitic quartz simple shear zone: the significant roles of dauphine twinning and misorientation," *Geological Society, London, Special Publications*, vol. 224, pp. 39–61, 2004.

[87] L. Menegon, S. Piazolo, and G. Pennacchioni, "The effect of Dauphiné twinning on plastic strain in quartz," *Contributions to Mineralogy and Petrology*, vol. 161, no. 4, pp. 635–652, 2011.

[88] J. M. Rahl, A. J. McGrew, J. A. Fox, J. R. Latham, and T. Gabrielson, "Rhomb-dominated crystallographic preferred orientations in incipiently deformed quartz sandstones: a potential paleostress indicator for quartz-rich rocks," *Geology*, vol. 46, no. 3, pp. 195–198, 2018.

[89] G. Lister, "Discussion: crossed-girdle c-axis fabrics in quartzites plastically deformed by plane strain and progressive simple shear," *Tectonophysics*, vol. 39, no. 1-3, pp. 51–54, 1977.

[90] J. Kruhl, "Reply: prism-and basal-plane parallel subgrain boundaries in quartz: a microstructural geothermobarometer," *Journal of Metamorphic Geology*, vol. 16, pp. 142–146, 1998.

[91] R. Law, "Deformation thermometry based on quartz c-axis fabrics and recrystallization microstructures: a review," *Journal of Structural Geology*, vol. 66, pp. 129–161, 2014.

[92] N. Hunter, R. Weinberg, C. Wilson, and R. Law, "A new technique for quantifying symmetry and opening angles in quartz c-axis pole figures: implications for interpreting the kinematic and thermal properties of rocks," *Journal of Structural Geology*, vol. 112, pp. 1–6, 2018.

[93] F. M. Faleiros, R. Moraes, M. Pavan, and G. A. C. Campanha, "A new empirical calibration of the quartz c-axis fabric opening-angle deformation thermometer," *Tectonophysics*, vol. 671, pp. 173–182, 2016.

[94] Y. Zhang, B. Hobbs, and M. Jessell, "The effect of grain-boundary sliding on fabric development in polycrystalline

aggregates," *Journal of Structural Geology*, vol. 16, no. 9, pp. 1315–1325, 1994.

[95] Z. Jiang, D. J. Prior, and J. Wheeler, "Albite crystallographic preferred orientation and grain misorientation distribution in a low-grade mylonite: implications for granular flow," *Journal of Structural Geology*, vol. 22, no. 11-12, pp. 1663–1674, 2000.

[96] R. Kilian, R. Heilbronner, and H. Stünitz, "Quartz grain size reduction in a granitoid rock and the transition from dislocation to diffusion creep," *Journal of Structural Geology*, vol. 33, no. 8, pp. 1265–1284, 2011.

[97] J. M. Rahl and P. Skemer, "Microstructural evolution and rheology of quartz in a mid-crustal shear zone," *Tectonophysics*, vol. 680, pp. 129–139, 2016.

[98] A. J. Cross and P. Skemer, "Ultramylonite generation via phase mixing in high-strain experiments," *Journal of Geophysical Research: Solid Earth*, vol. 122, no. 3, pp. 1744–1759, 2017.

[99] C. Truesdell, "Two measures of vorticity," *Journal of Rational Mechanics and Analysis*, vol. 2, pp. 173–217, 1953.

[100] H. Fossen and B. Tikoff, "The deformation matrix for simultaneous simple shearing, pure shearing and volume change, and its application to transpression-transtension tectonics," *Journal of Structural Geology*, vol. 15, no. 3-5, pp. 413–422, 1993.

[101] R. Law, M. P. Searle, and R. L. Simpson, "Strain, deformation temperatures and vorticity of flow at the top of the greater Himalayan slab, Everest massif, Tibet," *Journal of the Geological Society of London*, vol. 161, no. 2, pp. 305–320, 2004.

[102] P. Xypolias, "Vorticity analysis in shear zones: a review of methods and applications," *Journal of Structural Geology*, vol. 32, no. 12, pp. 2072–2092, 2010.

[103] S. R. Wallis, J. P. Platt, and S. D. Knott, "Recognition of syn-convergence extension in accretionary wedges with examples from the Calabrian arc and the eastern Alps," *American Journal of Science*, vol. 293, no. 5, pp. 463–494, 1993.

[104] C. W. Passchier, "Stable positions of rigid objects in non-coaxial flow—a study in vorticity analysis," *Journal of Structural Geology*, vol. 9, no. 5-6, pp. 679–690, 1987.

[105] S. E. Johnson, H. J. Lenferink, N. A. Price et al., "Clast-based kinematic vorticity gauges: the effects of slip at matrix/clast interfaces," *Journal of Structural Geology*, vol. 31, no. 11, pp. 1322–1339, 2009.

[106] C. Li and D. Jiang, "A critique of vorticity analysis using rigid clasts," *Journal of Structural Geology*, vol. 33, pp. 203–219, 2011.

[107] V. G. Toy, D. J. Prior, R. J. Norris, and A. F. Cooper, "Relationships between kinematic indicators and strain during syn-deformational exhumation of an oblique slip, transpressive, plate boundary shear zone: the Alpine Fault, New Zealand," *Earth and planetary science letters*, vol. 333-334, pp. 282–292, 2012.

[108] V. G. Toy, R. J. Norris, D. J. Prior, M. Walrond, and A. F. Cooper, "How do lineations reflect the strain history of transpressive shear zones? The example of the active Alpine Fault zone, New Zealand," *Journal of Structural Geology*, vol. 50, pp. 187–198, 2013.

[109] J. A. D. Connolly, "Computation of phase equilibria by linear programming: a tool for geodynamic modeling and its application to subduction zone decarbonation," *Earth and Planetary Science Letters*, vol. 236, no. 1-2, pp. 524–541, 2005.

[110] T. J. Holland and R. Powell, "An internally consistent thermodynamic data set for phases of petrological interest," *Journal of Metamorphic Geology*, vol. 16, no. 3, pp. 309–343, 1998.

[111] R. W. White, R. Powell, T. J. B. Holland, T. E. Johnson, and E. C. R. Green, "New mineral activity-composition relations for thermodynamic calculations in metapelitic systems," *Journal of Metamorphic Geology*, vol. 32, no. 3, pp. 261–286, 2014.

[112] E. Auzanneau, M. W. Schmidt, D. Vielzeuf, and J. A. D Connolly, "Titanium in phengite: a geobarometer for high temperature eclogites," *Contributions to Mineralogy and Petrology*, vol. 159, no. 1, pp. 1–24, 2010.

[113] R. Coggon and T. J. B. Holland, "Mixing properties of phengitic micas and revised garnet–phengite thermobarometers," *Journal of Metamorphic Geology*, vol. 20, no. 7, pp. 683–696, 2002.

[114] M. L. Fuhrman and D. H. Lindsley, "Ternary-feldspar modeling and thermometry," *American Mineralogist*, vol. 73, pp. 201–215, 1988.

[115] J. M. Montel, S. Foret, M. Veschambre, C. Nicollet, and A. Provost, "Electron microprobe dating of monazite," *Chemical Geology*, vol. 131, no. 1-4, pp. 37–53, 1996.

[116] K. R. Ludwig, *Isoplot/Ex version 4.15, a Geochronological Toolkit for Microsoft Excel*, vol. 4, Berkeley Geochronology Center Special Publication, Berkeley, California, 2012.

[117] F. S. Spear, J. M. Pyle, and D. Cherniak, "Limitations of chemical dating of monazite," *Chemical Geology*, vol. 266, no. 3-4, pp. 218–230, 2009.

[118] J. L. Crowley, N. Chatterjee, S. A. Bowring, P. J. Sylvester, J. S. Myers, and M. P. Searle, "U–(Th)–Pb dating of monazite and xenotime by EPMA, LA-ICPMS, and IDTIMS: examples from Yilgarn craton and Himalayas," *15th Annual Goldschmidt Conference Abstracts*, p. A19, 2005.

[119] N. Prabhakar, "Resolving poly-metamorphic Paleoarchean ages by chemical dating of monazites using multi-spectrometer U, Th and Pb analyses and sub-counting methodology," *Chemical Geology*, vol. 347, pp. 255–270, 2013.

[120] D. J. Cherniak, E. B. Watson, M. Grove, and T. M. Harrison, "Pb diffusion in monazite: a combined RBS/SIMS study," *Geochimica et Cosmochimica Acta*, vol. 68, no. 4, pp. 829–840, 2004.

[121] E. Gardes, J. M. Montel, A. M. Seydoux-Guillaume, and R. Wirth, "Pb diffusion in monazite: new constraints from the experimental study of $Pb^{2+} \Leftrightarrow Ca^{2+}$ interdiffusion," *Geochimica et Cosmochimica Acta*, vol. 71, no. 16, pp. 4036–4043, 2007.

[122] E. Gardes, O. Jaoul, J. M. Montel, A. M. Seydoux-Guillaume, and R. Wirth, "Pb diffusion in monazite: an experimental study of $Pb^{2+} + Th^{4+} \Leftrightarrow 2Nd^{3+}$ interdiffusion," *Geochimica et Cosmochimica Acta*, vol. 70, no. 9, pp. 2325–2336, 2006.

[123] T. D. Hoisch, M. T. Wells, and M. Grove, "Age trends in garnet-hosted monazite inclusions from upper amphibolite facies schist in the northern Grouse Creek mountains, Utah," *Geochimica et Cosmochimica Acta*, vol. 72, no. 22, pp. 5505–5520, 2008.

[124] S. Rekha, A. Bhattacharya, and N. Chatterjee, "Tectonic restoration of the Precambrian crystalline rocks along the west coast of India: correlation with eastern Madagascar in East Gondwana," *Precambrian Research*, vol. 252, pp. 191–208, 2014.

[125] S. Rekha, T. A. Viswanath, A. Bhattacharya, and N. Prabhakar, "Meso/Neoarchean crustal domains along the

north Konkan coast, western India: the Western Dharwar craton and the Antongil-Masora Block (NE Madagascar) connection," *Precambrian Research*, vol. 233, pp. 316–336, 2013.

[126] J. H. Kruhl, "Prism- and basal-plane parallel subgrain boundaries in quartz: a microstructural geothermobarometer," *Journal of Metamorphic Geology*, vol. 14, no. 5, pp. 581–589, 1996.

[127] S. R. Garlick and L. P. Gromet, "Diffusion creep and partial melting in high temperature mylonitic gneisses, Hope Valley shear zone, New England Appalachians, USA," *Journal of Metamorphic Geology*, vol. 22, no. 1, pp. 45–62, 2004.

[128] R. H. Vernon, S. E. Johnson, and E. A. Melis, "Emplacement-related microstructures in the margin of a deformed pluton: the San José tonalite, Baja California, México," *Journal of Structural Geology*, vol. 26, no. 10, pp. 1867–1884, 2004.

[129] A. Nicolas, "Kinematics in magmatic rocks with special reference to Gabbros," *Journal of Petrology*, vol. 33, no. 4, pp. 891–915, 1992.

[130] A. Berger and C. L. Rosenberg, "Preservation of chemical residue-melt equilibria in natural anatexite: the effects of deformation and rapid cooling," *Contributions to Mineralogy and Petrology*, vol. 144, no. 4, pp. 416–427, 2003.

[131] S. Bhadra, S. Das, and A. Bhattacharya, "Shear zone-hosted Migmatites (eastern India): the role of dynamic melting in the generation of REE-depleted felsic melts, and implications for disequilibrium melting," *Journal of petrology*, vol. 48, no. 3, pp. 435–457, 2007.

[132] L. Block and L. H. Royden, "Core complex geometries and regional scale flow in the lower crust," *Tectonics*, vol. 9, no. 4, pp. 557–567, 1990.

[133] B. J. Darby, G. A. Davis, X. Zhang, F. Wu, S. Wilde, and J. Yang, "The newly discovered Waziyu metamorphic core complex, Yiwulü Shan, western Liaoning Province, Northwest China," *Dixue Qianyuan(Earth Science Frontiers)*, vol. 11, no. 3, pp. 145–156, 2004.

[134] E. D. Humphreys, "Post-Laramide removal of the Farallon slab, western United States," *Geology*, vol. 23, no. 11, pp. 987–990, 1995.

[135] T. Wang, Y. Zheng, J. Zhang et al., "Pattern and kinematic polarity of late Mesozoic extension in continental NE Asia: perspectives from metamorphic core complexes," *Tectonics*, vol. 30, article 6007, 2011.

[136] C. M. Bailey and E. L. Eyster, "General shear deformation in the Pinaleño Mountains metamorphic core complex, Arizona," *Journal of Structural Geology*, vol. 25, no. 11, pp. 1883–1892, 2003.

[137] J. Lee, E. L. Miller, and J. F. Sutter, "Ductile strain and metamorphism in an extensional tectonic setting: a case study from the northern Snake Range, Nevada, USA," in *Continental Extensional Tectonics*, M. P. Coward, J. F. Dewey, and P. L. Hancock, Eds., vol. 28, pp. 267–298, Geological Society of London Special Publication, 1987.

[138] M. L. Wells and R. W. Allmendinger, "An early history of pure shear in the upper plate of the raft river metamorphic core complex: black Pine Mountains, southern Idaho," *Journal of Structural Geology*, vol. 12, no. 7, pp. 851–867, 1990.

[139] F. Gervais, L. Nadeau, and M. Malo, "Migmatitic structures and solid-state diapirism in ortho-gneiss domes, in eastern Grenville Province, Canada," in *Gneiss Domes in Orogeny*, D. Whitney, C. Teyssier, and C. S. Siddoway, Eds., vol. 380,

pp. 359–378, Geological Society of America Special Paper, 2004.

[140] S. R. Brown, G. D. M. Andrews, and H. D. Gibson, "Corrugated architecture of the Okanagan Valley shear zone and the Shuswap metamorphic complex, Canadian cordillera," *Lithosphere*, vol. 8, no. 4, pp. 412–421, 2016.

[141] A. Chauvet and M. Séranne, "Extension-parallel folding in the Scandinavian Caledonides: implications for late-orogenic processes," *Tectonics*, vol. 238, no. 1-4, pp. 31–54, 1994.

[142] J. E. Spencer and S. J. Reynolds, "Tectonics of mid-tertiary extension along a transect through west Central Arizona," *Tectonics*, vol. 10, no. 6, pp. 1204–1221, 1991.

[143] J. S. Singleton, "Development of extension-parallel corrugations in the buckskin-rawhide metamorphic core complex, west-Central Arizona," *Geological Society of America Bulletin*, vol. 125, no. 3-4, pp. 453–472, 2013.

[144] H. Fossen and B. Tikoff, "Extended models of transpression and transtension, and application to tectonic settings," *Geological Society, London, Special Publications*, vol. 135, no. 1, pp. 15–33, 1998.

[145] H. Fossen, B. Tikoff, and C. Teyssier, "Strain modeling of transpressional and transtensional deformation," *Norsk Geologisk Tidsskrift*, vol. 74, pp. 134–145, 1994.

[146] H. Fossen, C. Teyssier, and D. L. Whitney, "Transtensional folding," *Journal of Structural Geology*, vol. 56, pp. 89–102, 2013.

[147] D. Grujic and N. Mancktelow, "Folds with axes parallel to the extension direction: an experimental study," *Journal of Structural Geology*, vol. 17, no. 2, pp. 279–291, 1995.

[148] P.-Y. Robin and A. R. Cruden, "Strain and vorticity patterns in ideally ductile transpression zones," *Journal of Structural Geology*, vol. 16, no. 4, pp. 447–466, 1994.

[149] R. Dias and A. Ribeiro, "Constriction in a transpressive regime: an example in the Iberian branch of the Ibero-Armorican arc," *Journal of Structural Geology*, vol. 16, no. 11, pp. 1543–1554, 1994.

[150] D. J. Sanderson and W. R. D. Marchini, "Transpression," *Journal of Structural Geology*, vol. 6, no. 5, pp. 449–458, 1984.

[151] A. J. Watkinson, "Multilayer folds initiated in bulk plane strain, with the axis of no change perpendicular to the layering," *Tectonophysics*, vol. 28, no. 3, pp. T7–T11, 1975.

[152] W. M. Schwerdtner, "A Scale problem in paleo-strain analysis," *Tectonophysics*, vol. 16, no. 1-2, pp. 47–54, 1973.

[153] C. W. Passchier and J. P. Platt, "Shear zone junctions: of zippers and freeways," *Journal of Structural Geology*, vol. 95, pp. 188–202, 2017.

[154] S. K. Ghosh, "Types of transpressional and transtensional deformation," in *Geological Society of America Memoir*, H. A. Koyi and N. Mancktelow, Eds., vol. 193, pp. 1–20, 2001.

[155] C. Fernandez and M. Diaz-Azpiroz, "Triclinic transpression zones with inclined extrusion," *Journal of Structural Geology*, vol. 31, no. 10, pp. 1255–1269, 2009.

[156] O. Vanderhaeghe and C. Teyssier, "Partial melting and flow of orogens," *Tectonophysics*, vol. 342, no. 3-4, pp. 451–472, 2001.

[157] G. S. Lister and S. L. Baldwin, "Plutonism and the origin of metamorphic core complexes," *Geology*, vol. 21, no. 7, pp. 607–610, 1993.

[158] T. Parsons and G. A. Thompson, "Does magmatism influence low-angle normal faulting?," *Geology*, vol. 21, no. 3, pp. 247–250, 1993.

[159] M. Bregar, A. Bauernhofer, K. Pelz, U. Kloetzli, H. Fritz, and P. Neumayr, "A late Neoproterozoic magmatic core complex in the Eastern Desert of Egypt: emplacement of granitoids in a wrench-tectonic setting," *Precambrian Research*, vol. 118, no. 1-2, pp. 59–82, 2002.

[160] W. R. Buck, "Flexural rotation of normal faults," *Tectonics*, vol. 7, no. 5, pp. 959–973, 1988.

[161] J. M. Martínez-Martínez, J. I. Soto, and J. C. Balanyá, "Orthogonal folding of extensional detachments: structure and origin of the Sierra Nevada elongated dome (Betics, SE Spain)," *Tectonics*, vol. 21, no. 3, pp. 3-1–3-20, 2002.

[162] W. M. Behr and J. P. Platt, "Rheological evolution of a Mediterranean subduction complex," *Journal of Structural Geology*, vol. 54, pp. 136–155, 2013.

[163] R. R. Jones, R. E. Holdsworth, and W. Bailey, "Lateral extrusion in transpression zones: the importance of boundary conditions," *Journal of Structural Geology*, vol. 19, no. 9, pp. 1201–1217, 1997.

[164] R. R. Jones, R. E. Holdsworth, P. Clegg, K. McCaffrey, and E. Tavarnelli, "Inclined transpression," *Journal of Structural Geology*, vol. 26, no. 8, pp. 1531–1548, 2004.

[165] R. R. Jones, R. E. Holdsworth, M. Hand, and B. Goscombe, "Ductile extrusion in continental collision zones: ambiguities in the definition of channel flow and its identification in ancient orogens," in *Channel Flow, Ductile Extrusion and Exhumation in Continental Collision Zones*, R. D. Law, M. P. Searle, and L. Goidin, Eds., vol. 268, pp. 201–219, Geological Society of London Special Publication, 2006.

[166] S. Lin, D. Jiang, and P. F. Williams, "Transpression (or transtension) zones of triclinic symmetry: natural example and theoretical modeling," in *Continental Transpressional and Transtensional Tectonics*, R. E. Holdsworth, R. A. Strachran, and J. F. Dewey, Eds., vol. 135, pp. 41–57, Geological Society of London Special Publication, 1998.

[167] J. Jacobs and R. Thomas, "Himalayan-type indenter-escape tectonics model for the southern part of the late Neoproterozoic-early Paleozoic east African-Antarctic orogen," *Geology*, vol. 32, no. 8, pp. 721–724, 2004.

[168] Y. D. Kuiper, S. Lin, and C. O. Bohm, "Himalayan-type escape tectonics along the superior boundary zone in Manitoba, Canada," *Precambrian Research*, vol. 187, no. 3-4, pp. 248–262, 2011.

[169] P. Molnar and P. Tapponier, "Cenozoic tectonics of Asia: effects of a continental Collision: features of recent continental tectonics in Asia can be interpreted as results of the India-Eurasia collision," *Science*, vol. 189, no. 4201, pp. 419–426, 1975.

[170] L. Ratschbacher, O. Merle, P. Davy, and P. Cobbold, "Lateral extrusion in the eastern Alps, part 1: boundary conditions and experiments scaled for gravity," *Tectonics*, vol. 10, no. 2, pp. 245–256, 1991.

[171] K. Gessner, C. Wijns, and L. Moresi, "Significance of strain localization in the lower crust for structural evolution and thermal history of metamorphic core complexes," *Tectonics*, vol. 26, no. 2, 2007.

[172] D. Grujic, L. S. Hollister, and R. R. Parrish, "Himalayan metamorphic sequence as an orogenic channel: insight from Bhutan," *Earth and Planetary Science Letters*, vol. 198, no. 1-2, pp. 177–191, 2002.

[173] G. Casale, J. S. F. Levine, T. D. Craig, and C. Stewart, "Timing and deformation conditions of the Tallulah Falls dome, NE. Georgia: Implications for the Alleghanian orogeny," *Geological Society of America Bulletin*, vol. 129, pp. B31595.1–B3151208, 2017.

[174] Geological Survey of India, *District Resource Map-Devghar*, Geological Survey of India, Jharkhand, 2001.

[175] Geological Survey of India, *District Resource Map-Giridih*, Geological Survey of India, Jharkhand, 2006.

[176] Geological Survey of India, *District Resource Map-Dumka*, Geological Survey of India, Jharkhand, 2009.

[177] Geological Survey of India, *District Resource Map-Banka*, Geological Survey of India, Bihar, 2012.

[178] Geological Survey of India, *District Resource Map-Jamui*, Geological Survey of India, Bihar, 2001.